

BOWIE-ALIGN: Sub-solar C/O ratio and metallicity atmosphere of the misaligned hot Jupiter HAT-P-30 b

Alastair B. Claringbold^{1,2}*, Chloe E. Fisher^{1,3}, James Kirk^{1,4}, Eva-Maria Ahrer^{1,5}, Anna B. T. Penzlin^{1,6,4}, Daniel P. Thorngren^{1,7}, Mercedes López-Morales^{1,8}, Peter J. Wheatley^{1,2}, Lili Alderson^{1,9}, Richard A. Booth^{1,10}, Duncan A. Christie^{1,5}, Charlotte Fairman^{1,11}, Nathan J. Mayne^{1,12}, Mason McCormack^{1,13}, Annabella Meech^{1,14}, James E. Owen^{1,4}, Vatsal Panwar^{1,12}, Denis E. Sergeev^{1,11}, Daniel Valentine^{1,11}, Hannah R. Wakeford^{1,11}, Maria Zamyatina^{1,12}

¹Department of Physics, University of Warwick, Gibbet Hill Road, Coventry CV4 7AL, UK

²Centre for Exoplanets and Habitability, University of Warwick, Gibbet Hill Road, Coventry CV4 7AL, UK

³Department of Physics, University of Oxford, Denys Wilkinson Building, Keble Road, Oxford, OX1 3RH, United Kingdom

⁴Department of Physics, Imperial College London, Prince Consort Road, SW7 2AZ, London, UK

⁵Max Planck Institute for Astronomy (MPIA), Königstuhl 17, 69117 Heidelberg, Germany

⁶Ludwig-Maximilians-Universität München, Universitäts-Sternwarte, Scheinerstr. 1, 81679 München, Germany

⁷Department of Physics and Astronomy, Johns Hopkins University, Baltimore, MD 21218, USA

⁸Space Telescope Science Institute, 3700 San Martin Drive, Baltimore MD 21218, USA

⁹Department of Astronomy, Cornell University, 122 Sciences Drive, Ithaca, NY 14853, USA

¹⁰School of Physics and Astronomy, University of Leeds, Leeds, LS2 9JT

¹¹School of Physics, HH Wills Physics Laboratory, University of Bristol, Tyndall Avenue, Bristol BS8 1TL, UK

¹²Department of Physics and Astronomy, Faculty of Environment, Science and Economy, University of Exeter, Exeter EX4 4QL, UK

¹³Department of Astronomy & Astrophysics, University of Chicago, Chicago, IL 60637, USA

¹⁴Center for Astrophysics | Harvard & Smithsonian, 60 Garden St, Cambridge, MA 02138, USA

Accepted XXX. Received YYY; in original form ZZZ

ABSTRACT

We present the JWST NIRSpec/G395H transmission spectrum of the misaligned hot Jupiter HAT-P-30b from 2.8–5.2 μ m as part of the BOWIE-ALIGN survey, a comparative survey designed to probe the link between planet formation and atmospheric composition in samples of misaligned and aligned hot Jupiters orbiting F-type stars. Through independent data reductions and retrieval analyses, we find evidence for absorption features of H₂O and CO₂ in the atmosphere of HAT-P-30b. Our retrieved abundances are consistent with equilibrium chemistry, from which we infer a sub-solar C/O ratio (0.16–0.45), and sub-solar and sub-stellar metallicity (0.2–0.8×solar, compared to a stellar metallicity of 1.1–1.6×solar), with muted spectral features. This composition challenges formation models of continuous migration and accretion within a steady disc of stellar metallicity, and could be the result of low C/O ratio gas accretion within the water ice line, low metallicity accretion due to the trapping of volatiles further out in the disc, or the combined accretion of low metallicity gas and carbon-poor solids.

Key words: exoplanets – planets and satellites: gaseous planets, atmospheres, composition – techniques: spectroscopic

1 INTRODUCTION

The idea that the composition of an exoplanet atmosphere may conceal clues as to its formation location and migration history has been a key driver for the characterization of exoplanets. With the unparalleled precision and near-infrared wavelength coverage afforded by JWST, it is now possible to accurately measure relative elemental abundances in exoplanet atmospheres (e.g., JWST Transiting Exoplanet Community Early Release Science Team et al. 2023; Ahrer

et al. 2023; Alderson et al. 2023; Feinstein et al. 2023; Rustamkulov et al. 2023). In principle, we can use the C/O ratio to infer where a planet formed relative to the ice lines of H₂O, CO₂, and CO in the protoplanetary disc (Öberg et al. 2011).

In practice, relating the atmospheric composition for a single planet to its formation history challenges this simple picture, with numerous physical processes obscuring the relationship between formation models and observed atmospheres. This is because, fundamentally, modelling planet formation includes a high dimensionality of poorly constrained parameters, including temperature profile, dust-to-gas ratio, and composition of the protoplanetary disc (e.g.,

* E-mail: alastair.claringbold@warwick.ac.uk

Mollière et al. 2022). This can be additionally complicated by including physical processes important during formation, such as relative accretion of gas and solid (Espinoza et al. 2017), the evolution of ice lines (Morbidelli et al. 2016; Owen 2020), the drift of volatile-carrying solids (Booth et al. 2017; Schneider & Bitsch 2021), and the trapping of volatiles within ice (Ligterink et al. 2024), as well as the complexity arising due to migration, as planets can accrete in multiple environments through their evolution. Observations of protoplanetary discs have also revealed them to be diverse objects, with their radial composition varying between host stars (Law et al. 2021a; Law et al. 2021b). Furthermore, directly relating a planet’s atmospheric composition to its bulk elemental ratios is non-trivial, with potential impacts from cloud formation (Helling et al. 2016) or enrichment of an atmosphere uncoupled from the interior (Müller & Helled 2024).

As demonstrated by Penzlin & Booth et al. (2024), while any single planet is a poor tracer of planet formation, we can use populations of exoplanets with similar dynamical properties implying shared formation histories to test whether atmospheric composition traces planet formation. In particular, Penzlin & Booth et al. (2024) show how planets which underwent disc-migration should be chemically distinct from planets that underwent disc-free migration, with the precise nature of this distinction depending upon the behaviour of accreted silicates and the dominant carbon-bearing species within the disc. We can leverage the two distinct populations of aligned hot Jupiters, that likely migrated through the disc, and misaligned hot Jupiters, that likely underwent high-eccentricity migration after disc dispersal (Rasio & Ford 1996; Wu & Murray 2003; Muñoz et al. 2016). Comparing these two dynamically distinct populations we can test the predictions of Penzlin & Booth et al. (2024).

This is precisely the goal of the BOWIE-ALIGN survey (A spectral Light Investigation into gas Giant origiNs; JWST GO 3838; PIs: Kirk & Ahrer), by spectroscopically characterizing eight planets: four aligned hot Jupiters believed to have migrated through the disc, and four misaligned hot Jupiters believed to have migrated via high-eccentricity migration (Kirk et al. 2024a). All eight planets orbit stars above the Kraft Break ($T_{\text{eff}} \gtrsim 6100$ K), an observed shift in rotation rates attributed to much thinner surface convective zones than cooler stars causing less efficient magnetic breaking (Kraft 1967; Beyer & White 2024). Realignment of hot Jupiters due to tidal interactions with the star is unlikely to occur above the Kraft break, fitting the observation that hot Jupiters around cooler stars tend to have low stellar obliquities (Winn et al. 2010; Albrecht et al. 2012). This ensures the aligned planets in the BOWIE-ALIGN sample are not aligned due to re-alignment of the star, and are instead likely aligned due to migration through the disc.

The transmission spectra of three planets from the BOWIE-ALIGN sample have been published to date. The misaligned planet WASP-15 b was found to host a super-stellar metallicity atmosphere with a solar C/O ratio and evidence of SO_2 absorption (Kirk et al. 2025). This combination of atmospheric properties was tentatively attributed to late planetesimal accretion. Meanwhile the aligned planet TrES-4 b was found to instead host a sub-stellar metallicity atmosphere with a sub-solar C/O ratio, challenging traditional planet formation models by suggesting either low C/O ratio gas accretion, or a combination of gas and carbon-poor solid accretion (Meech et al. 2025). Another aligned planet, KELT-7 b, was found to have very weak spectral features due to either a high cloud deck or low atmospheric metallicity, limiting the ability to place constraints on the C/O ratio and metallicity (Ahrer et al. *submitted*).

In this work we present the JWST NIRSpec/G395H transmission spectrum of HAT-P-30 b, a misaligned hot Jupiter in the BOWIE-

Table 1. System parameters for HAT-P-30 b. References are for: [1] Johnson et al. (2011), [2] Bonomo et al. (2017), [3] Blažek et al. (2022), [4] Ivshina & Winn (2022), and [5] Cegla et al. (2023).

Parameter	Value	Reference
<i>Stellar parameters</i>		
Mass, M_* (M_{\odot})	1.242 ± 0.041	[2]
Radius, R_* (R_{\odot})	1.215 ± 0.051	[2]
Effective Temperature, T_{eff} (K)	6304 ± 88	[1]
Age (Gyr)	$1.0^{+0.8}_{-0.5}$	[2]
Surface gravity, $\log g$ (cgs)	4.36 ± 0.04	[2]
Metallicity [Fe/H] (dex)	0.13 ± 0.08	[2]
<i>Planetary parameters</i>		
Mass, M_p (M_{Jup})	$0.746^{+0.020}_{-0.021}$	[2]
Radius, R_p (R_{Jup})	1.417 ± 0.033	[3]
Equ. Temperature, T_{eq} (K)	1630 ± 42	[3]
Gravity, (ms^{-2})	9.2 ± 0.5	
Orbital period, P (days)	2.8106013 ± 0.0000006	[4]
Obliquity, λ (degrees)	$70.5^{+2.9}_{-2.8}$	[5]

ALIGN programme, with a measured obliquity of $70.5^{+2.9}_{-2.8}$ ° (Cegla et al. 2023). HAT-P-30 b, also known as WASP-51 b, has a mass of $0.746 \pm 0.021 M_{\text{Jup}}$ (Bonomo et al. 2017), a radius of $1.42 \pm 0.03 R_{\text{Jup}}$, equilibrium temperature of 1630 ± 42 K (Blažek et al. 2022), and an orbital period of 2.8106013 ± 0.0000006 days (Ivshina & Winn 2022). We include a full summary of our adopted system parameters in Table 1.

We describe the JWST observations in Section 2, and the data reduction and light curve fitting in Section 3. To derive the atmospheric composition of HAT-P-30 b, we outline an atmospheric retrieval analysis to interpret the spectrum in Section 4. In Section 5, we use interior structure models to place constraints on the atmospheric composition and infer the bulk metallicity of HAT-P-30 b based on the system parameters. We include a discussion of the atmosphere of HAT-P-30 b and its relevance to its formation history in Section 6, and present our conclusions in Section 7.

2 OBSERVATIONS

We observed one transit of HAT-P-30b with JWST on 10 March 2024, 22:20:47 UT as part of the GO 3838 programme, using the NIRSpec instrument (Jakobsen et al. 2022) in Bright Object Time Series (BOTS) mode, with the G395H grating, F290LP filter, and SUB2048 subarray. This setup provides spectroscopy from $2.8 - 5.2 \mu\text{m}$ at a resolution of $R \sim 2700$, with a gap in coverage from $3.72 - 3.82 \mu\text{m}$ due to a physical gap between the NRS1 and NRS2 detectors. We use 26 groups per integration, with 925 integrations over 6.26 hours, including 2.25 hours during transit. We use a nearby faint star (2MASSJ08154583+0550218) for target acquisition in WATA mode with the SUB32 subarray and CLEAR filter.

3 DATA REDUCTION

We perform two independent data reductions, as prescribed by the BOWIE-ALIGN data analysis strategy found in Kirk et al. (2024a). We use two pipelines, Eureka! (Bell et al. 2022) and Tiberius (Kirk et al. 2017, 2021), for the data reduction, broadly following the methodology for other BOWIE-ALIGN targets WASP-15 b (Kirk et al. 2025) TrES-4 b (Meech et al. 2025), and KELT-7 b (Ahrer et al. 2025), with exact details of the spectral extraction and light curve fitting detailed below.

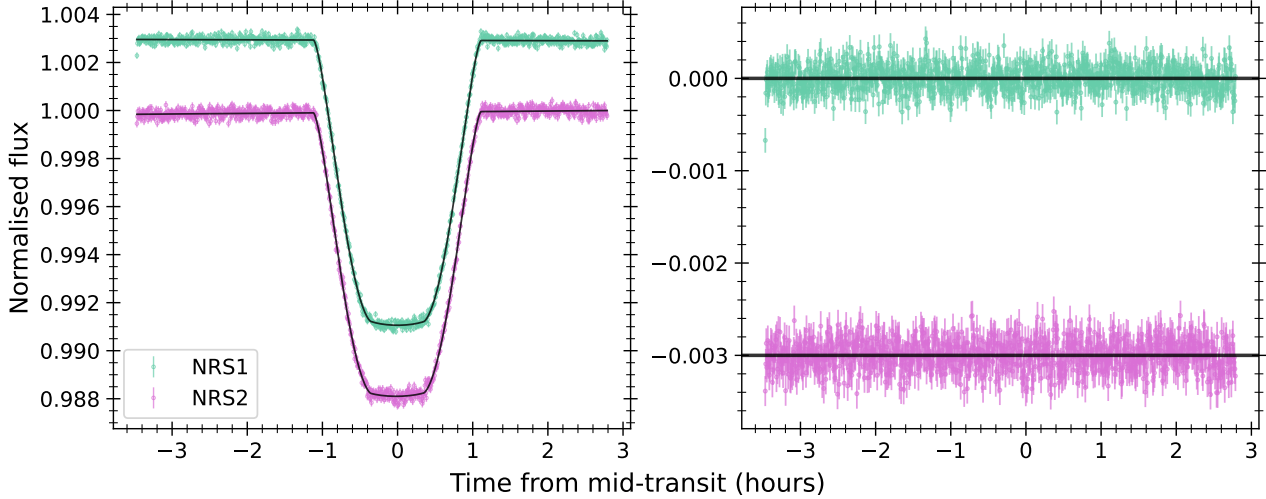


Figure 1. White light curves for HAT-P-30b for each detector, NRS1 (green) and NRS2 (magenta) from the Eureka data reduction (left) and the residuals from the light curve fits (right).

Table 2. The resulting system parameters from our fits to the individual JWST NIRSpec/G395H NRS1 and NRS2 white light curves, the system parameters from the combined fit to both the NRS1 and NRS2 data (Eureka only), and the weighted mean of both individual NRS1 and NRS2 fits (Tiberius only).

Pipeline	Instrument	T_0 (BJD)	R_p/R_*	a/R_*	i ($^{\circ}$)
Eureka!	NRS1	2460380.639378 \pm 0.000030	0.110156 \pm 0.000090	6.819 \pm 0.021	82.746 \pm 0.031
Eureka!	NRS2	2460380.639344 \pm 0.000034	0.10991 \pm 0.00011	6.799 \pm 0.018	82.717 \pm 0.026
Eureka!	Combined fit	2460380.639363 \pm 0.000018	0.109920 \pm 0.000067	6.791 \pm 0.009	82.699 \pm 0.013
Tiberius	NRS1	2460380.639369 \pm 0.000023	0.110265 \pm 0.000070	6.798 \pm 0.012	82.716 \pm 0.017
Tiberius	NRS2	2460380.639335 \pm 0.000029	0.109843 \pm 0.000088	6.782 \pm 0.017	82.690 \pm 0.021
Tiberius	Weighted mean	2460380.639356 \pm 0.000018	0.110101 \pm 0.000055	6.792 \pm 0.009	82.706 \pm 0.013

3.1 Eureka!

We conduct a data reduction of HAT-P-30 b using the open-source python package Eureka! (Bell et al. 2022), which has been used extensively for analysing JWST exoplanet transmission spectra (e.g., Ahrer et al. 2023; Moran et al. 2023; Alderson et al. 2024; Wallack et al. 2024; Xue et al. 2024; Teske et al. 2025).

3.1.1 Light curve extraction

We follow previous BOWIE-ALIGN analyses when conducting our Eureka! analysis. We start with the uncalibrated files and run Stage 1 and 2 of Eureka! which is wrapped around the `jwst` pipeline (version 1.12.2, CRDS context pmap: 1253), with the following common modifications: we apply a correction factor to the `jwst` superbias (group 1, smooth, window length of 30 pixels), we increase the `jump_rejection_threshold` to 10.0σ (e.g., see Alderson et al. 2023), we run a group-level column-by-column background subtraction (with an outlier rejection threshold of $3\times$ median), and we skip the `photom_step`. Note that in order to compute the bias scale factor and run the $1/f$ background subtraction we mask the trace using 10 pixels around the central trace.

In Stage 3, we extract the stellar spectrum for each integration. We apply a constant column-by-column background subtraction (excluding the 8/10 pixel area on both sides from the central trace pixel for NRS1/NRS2, respectively) using a 5-sigma threshold for outlier rejection along both the time and spatial axes. We extract the stellar spectrum using optimal spectral extraction (Horne 1986) with an aperture half-width of 4 pixels. We further manually mask columns

where the count is $> 15\sigma$ from a rolling mean of 20 pixels across the frame.

The extracted stellar spectra are binned in Stage 4 following the common BOWIE-ALIGN grid, at $R=100$ and $R=400$. We mask outliers $> 5\sigma$ on the rolling median (25 pixels) of the binned light curves.

3.1.2 Light curve fitting

We follow the commonly used procedure that the broadband white light curves for NRS1 and NRS2 are fitted first, using the transit depth R_p/R_* , the scaled stellar radius a/R_* , the mid-transit time T_0 , and inclination i as free parameters. We further fit for a baseline offset and a linear slope. The orbital period and eccentricity of HAT-P-30 b are fixed, to 2.8106 days (Ivshina & Winn 2022) and 0, respectively, and we fix the limb-darkening using the quadratic limb-darkening law and parameters u_1, u_2 . The limb-darkening values are computed for each bin in Eureka!‘s Stage 4 using ExoTiC-LD (Grant & Wakeford 2024) and the 3D Stagger grid (Magic et al. 2015), based on the stellar parameters from Table 1.

The best-fit parameters are derived using the Python Markov Chain Monte Carlo (MCMC) sampler `emcee` (Foreman-Mackey et al. 2013), using 50 walkers and 3000 steps (of which 1000 were discarded as burn-in steps). The retrieved parameters for HAT-P-30 b’s orbit based on the white light curve from NRS1 and NRS2 are in Table 2, with the light curve fits presented in Figure 1. For our spectroscopic NRS1 and NRS2 fits, we then fixed the orbital parameters ($a/R_*, i, T_0$) to the best-fit values by the NRS1 or NRS2 white light curves, respectively. We fix the limb-darkening parameters to

those calculated for each spectroscopic bin. Therefore, each spectroscopic light curve fit included three free parameters: the transit depth R_p/R_* and the parameters describing the baseline offset and linear slope term of the light curve. The resulting transmission spectra at $R = 100$ and $R = 400$ are displayed in Fig. 2.

We also perform a simultaneous fit to the white light curves from both detectors from which we derive the combined fit system parameters presented in Table 2. Using these system parameters to generate a transmission spectrum in the same manner causes negligible differences in the spectrum when compared to that generated with the individual system parameters for each detector, except for a minor vertical offset (with an average of 32 ppm for NRS1, 26 ppm for NRS2) with no slope or change of shape.

3.2 Tiberius

We also conduct a data reduction of HAT-P-30 b using Tiberius (Kirk et al. 2017, 2021), an open-source package for data reduction and light-curve fitting originally developed for ground-based exoplanet atmosphere transmission spectroscopy, now used extensively for JWST observations (e.g., Rustamkulov et al. 2023; Moran et al. 2023; Kirk et al. 2024b).

3.2.1 Light curve extraction

For our Tiberius reduction, we followed an identical process as used in our BOWIE-ALIGN analyses of WASP-15b (Kirk et al. 2025) and TrES-4b (Meech et al. 2025), and use the same pipeline version (Tiberius: v1.0.4, jwst: v1.8.2) and calibration reference files. We refer the reader to Kirk et al. (2025) for a detailed explanation of this process. In short, we perform stage 1 using a modified version of the jwst pipeline, skipping the jump_step and adding our own 1/f correction. Stage 2 is performed by Tiberius after our own custom bad pixel flagging and correction procedure (detailed in Kirk et al. 2025). We perform standard aperture photometry with an aperture full width of 8 pixels and perform an additional background subtraction at this stage, using a linear polynomial fitted to each pixel column after masking the 22 pixels centered on the stellar trace.

To construct our light curves, we use the same two binning schemes as in our other BOWIE-ALIGN papers, namely a lower resolution $R = 100$ wavelength grid and a higher resolution $R = 400$ wavelength grid. Our NRS1 light curves span a wavelength range of 2.75–3.72 μm with NRS2 spanning 3.82–5.18 μm .

3.2.2 Light curve fitting

For our light curve fits, we again follow an identical procedure to that detailed in Kirk et al. (2025). We fit our light curves with a quadratically limb-darkened analytic transit light curve (implemented through batman, Kreidberg 2015) multiplied by a linear-in-time polynomial. For our white light curve fits, the free parameters are the planet-to-star radius ratio (R_p/R_*), the planet's inclination (i), the semi-major axis to stellar radius ratio (a/R_*), the time of mid-transit (T_0), and the two parameters of the linear polynomial (c_1, c_2). We held the period fixed to 2.81060126 d (Ivshina & Winn 2022) and the eccentricity to 0¹. We fixed the limb darkening coefficients to the values found using the Stagger grid of 3D stellar atmosphere

¹ We also tested fixing eccentricity to 0.035 according to the results of Johnson et al. (2011) but found that this led to a negligible difference in the resulting transmission spectra with a median difference of 1.5 ppm.

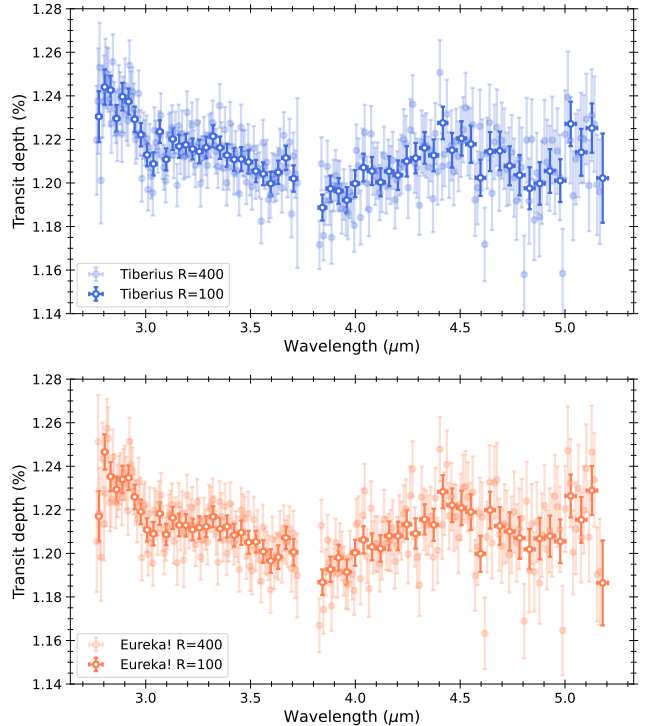


Figure 2. Transmission spectra of HAT-P-30 b from Tiberius (top) and Eureka! (bottom) data reductions, binned to spectral resolutions of $R = 400$ and $R = 100$.

models (Magic et al. 2015) as computed by ExoTiC-LD (Grant & Wakeford 2024) using the stellar parameters given in Table 1.

Our best-fitting system parameters are derived from the white light curves and are given in Table 2. These are the result of optimization using a Levenberg-Marquardt algorithm. Following the fitting of the white light curves, we fit our spectroscopic light curves with the same model setup but with the system parameters fixed to the weighted mean values as given in Table 2. The result of this was the transmission spectra shown in Fig. 2.

3.3 The transmission spectrum of HAT-P-30b

We present the transmission spectra obtained from each of our reduction pipelines at spectral resolutions of $R = 100$ and $R = 400$ in Fig. 2. While these reductions agree well in overall feature shape and depths (with a 7 ppm mean offset), we do find that the difference between the reductions depends linearly on wavelength, as depicted in Fig. 3. We perform a linear fit on the differences, demonstrating a difference in slope of 100 ppm across the whole spectrum. The light curve fitting, while performed independently for the two reductions, arrived at the same systematic models and used the same limb-darkening coefficients, only differing in the use of MCMC versus Levenberg-Marquardt, which has been demonstrated to not impact the results. While our derived Eureka! transmission spectrum uses a different approach to system parameters (using the system parameters from each detector individually) than the Tiberius spectrum (using the weighted mean), we verify this is not the cause of the difference by testing a Eureka! transmission spectrum using system parameters from a combined white light curve fit. This results in a near-identical transmission spectrum with no slope and mini-

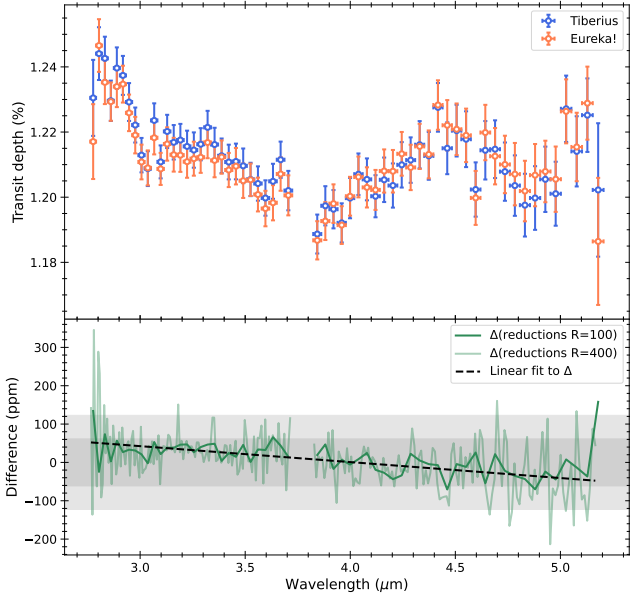


Figure 3. Comparison between transmission spectra obtained by our Tiberius and Eureka! reductions at $R = 100$, including the difference between the $R = 100$ and $R = 400$ spectra in green in the bottom panel. The shaded grey regions are the $1\times$ and $2\times$ the median transit depth uncertainty of the Eureka! $R = 100$ reduction. We find that the difference between reductions depends linearly on wavelength, with a mean offset of $+35$ ppm and -21 ppm in NRS1 and NRS2 respectively.

mal detector offset (~ 5 ppm). Due to the high impact parameter of HAT-P-30 b, the limb-darkening is fixed in both of our reductions.

A detailed investigation into differences in reduction method was performed for the previous BOWIE-ALIGN target WASP-15b (Kirk et al. 2025), finding that offset and slopes between the Tiberius and Eureka! reductions occur at the spectral extraction stage, as opposed to stage 1 extraction, system parameters, or limb-darkening coefficients. Understanding the difference between reductions is an ongoing effort for the field (e.g. Carter et al. 2024).

4 ATMOSPHERIC MODELLING

To interpret the Eureka! and Tiberius transmission spectra, we use a grid of simple 1D equilibrium forward models for an initial comparison to the data. We follow this with an atmospheric retrieval analysis to provide a detailed interpretation, independently implemented using the publicly available packages `petitRADTRANS` and `BeAR`. We detail the modelling setup and results of each package below.

4.1 `petitRADTRANS` forward models

We simulate the atmosphere of HAT-P-30 b with the `petitRADTRANS`² (v3.1.3, Mollière et al. 2019) package, assuming a 1D isothermal atmosphere and chemical equilibrium. In all cases we assume a H₂/He-dominated atmosphere, and include $R = 1000$ correlated- k line opacities from CO (Rothman et al. 2010), H₂O (Polyansky et al. 2018), CO₂ (Yurchenko et al. 2020), CH₄ (Yurchenko et al. 2017), H₂S (Azzam et al. 2016), SO₂ (Underwood

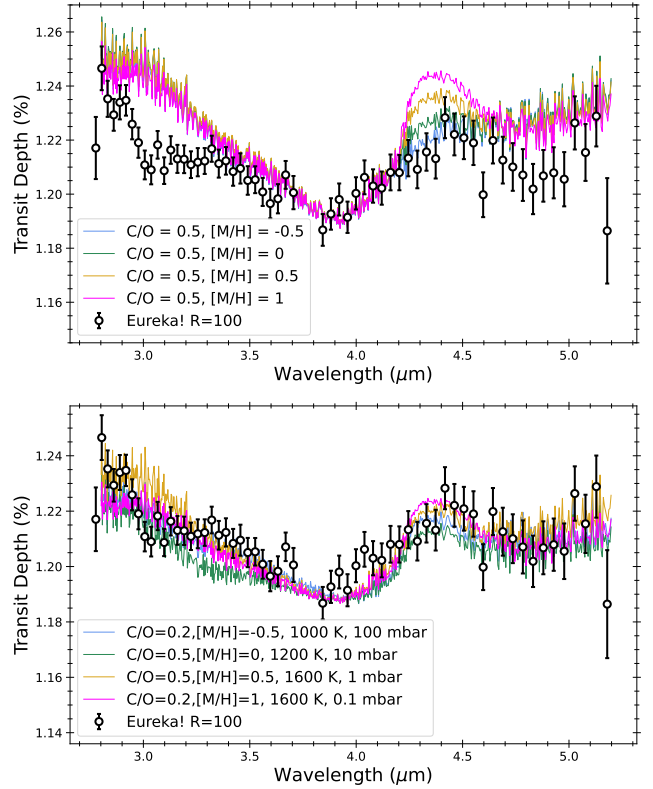


Figure 4. 1D isothermal chemical equilibrium forward models of HAT-P-30 b compared to the Eureka! $R = 100$ transmission spectrum. The left panel depicts cloud-free models with the isotherm temperature set to 1630 K, the equilibrium temperature of HAT-P-30 b. The right panel depicts a selection of models at different metallicities with comparable fits to the data using different C/O ratios, isotherm temperatures, and opaque grey cloud-top pressures, all noted in the legend. These models demonstrate that the spectral features of HAT-P-30 b are muted compared to those predicted by cloud-free models. The degeneracies between composition, temperature, and clouds highlighted in the right panel demonstrate the need for a full exploration of the parameter space using atmospheric retrievals to interpret the spectrum of HAT-P-30 b.

et al. 2016), SO (Brady et al. 2024), HCN (Barber et al. 2014), and NH₃ (Coles et al. 2019), as well as collisionally-induced absorption from H₂–H₂ and H₂–He (Borysow et al. 1988, 2001; Borysow 2002), and Rayleigh scattering from H₂ and He (Dalgarno & Williams 1962; Chan & Dalgarno 1965). We model the atmosphere using 100 log-spaced pressure layers from 10^{-6} to 10^2 bar.

We initially constructed a simple grid of cloud-free simulations with the temperature set to the equilibrium temperature, varying the C/O ratio from 0.2–1.0, and the log₁₀ metallicity relative to solar ([M/H]) from -1 to 2. These simple models demonstrate visibly stronger spectral features than those present in the observed spectra, highlighting that the spectral features are muted to some degree, as shown in the first panel of Fig. 4.

We then expanded this initial grid by including an opaque grey cloud deck at varying pressures (up to 0.1 mbar), and by reducing the isotherm temperature (down to 1000 K). By tuning the C/O ratio, isotherm temperature, and cloud-top pressure, we were able to create comparable, adequate fits to the data at a range of metallicities from 0.3 – 30× solar, presented in the second panel of Fig. 4. This exemplifies the strong degeneracies in atmospheric models, particularly given the limited wavelength coverage of G395H data, with only subtle differences between these fits mainly visible at $4.4\ \mu\text{m}$.

² <https://petitradtrans.readthedocs.io/en/latest/>

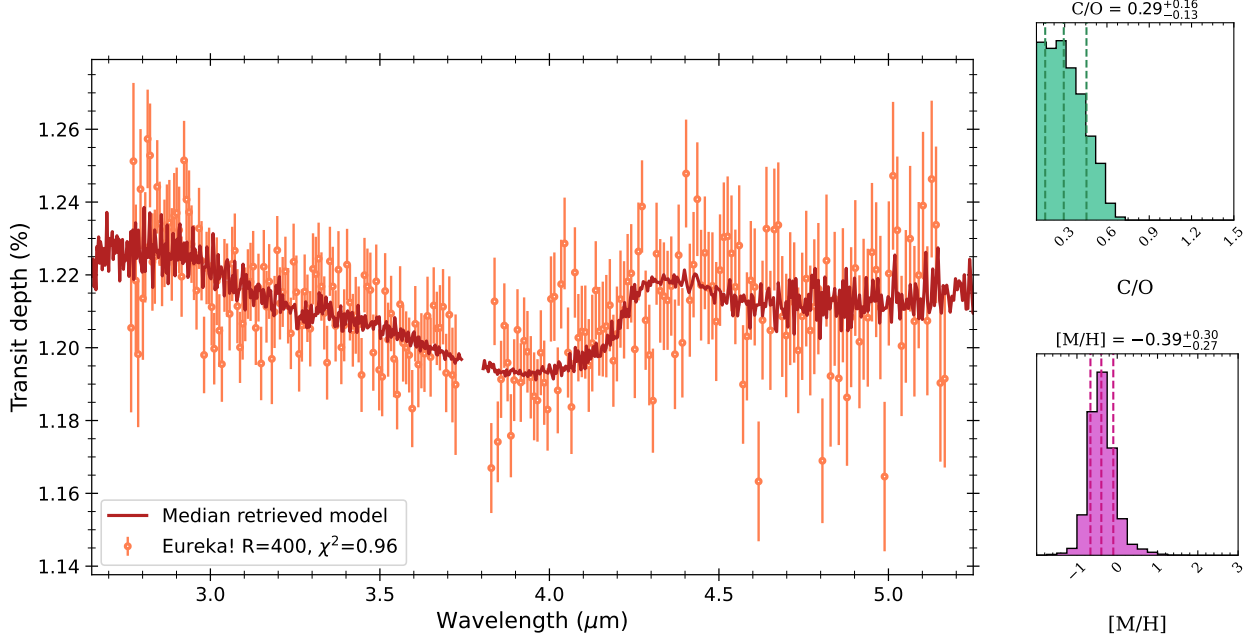


Figure 5. Median retrieved spectrum (red) of the Eureka! $R = 400$ data (orange) from the `petitRADTRANS` equilibrium chemistry retrieval with no offset, with the posterior probability distributions of C/O ratio and [M/H].

and $3.3\ \mu\text{m}$. Our ability to constrain the atmosphere of HAT-P-30 b by eye with a coarse forward model grid alone is therefore limited, and we turn to the statistical power offered by atmospheric retrievals and nested sampling to fully explore the model parameter space.

4.2 `petitRADTRANS` retrievals

We perform a variety of atmospheric retrievals on the HAT-P-30 b transmission spectrum with `petitRADTRANS` (Nasedkin et al. 2024), using a similar setup to that used to analyse the spectrum of the BOWIE-ALIGN targets WASP-15 b (Kirk et al. 2025) and TrES-4 b (Meech et al. 2025). `petitRADTRANS` explores the multi-dimensional model transmission spectrum parameter space using Bayesian nested sampling (Skilling 2004) implemented through `MultiNest` (Feroz & Hobson 2008) with `PyMultiNest` (Buchner et al. 2014). As with other BOWIE-ALIGN targets, we use three principle setups: equilibrium chemistry, free chemistry, and hybrid chemistry.

For all of our retrievals, we use the model setup properties and opacity sources described in Section 4.1. The stellar radius is fixed to the value of $1.215 R_\odot$ from Bonomo et al. (2017). For our standard retrieval setups, we assume an isothermal pressure-temperature profile with a wide uniform temperature prior of $500\text{--}3000\text{ K}$. We also adopt a Gaussian prior for the gravity based on the mass and radius (Bonomo et al. 2017), and a wide uniform prior for the planetary radius of $0.8\text{--}2.2 R_J$, defined at a reference pressure of 1 mbar. We parametrize the impact of aerosols by including a grey cloud deck, with a log-uniform prior on the cloud-top pressure from 10^{-6} bar to 10^2 bar .

We run our retrievals on the $R = 100$ and $R = 400$ transmission spectra from both the Eureka! and Tiberius reductions. We permit for an offset between NRS1 and NRS2, with a uniform prior of $\pm 200\text{ ppm}$. We determine the detection significances of different species by computing the difference in Bayesian evidence $\ln Z$ between the retrieval with all species included, and the retrieval with the considered species omitted, converted into a frequentist significance

value from the Bayes factor B_m via the p -value using $p = \frac{1}{1+B_m}$ (Jeffreys 1939). We summarise all of our retrieval results, including evidence and posteriors, in Table A1.

4.2.1 Equilibrium chemistry

In our equilibrium retrievals, we assume all the atmospheric species are in chemical equilibrium, with the abundances of CH_4 , CO_2 , CO , H_2O , H_2S , HCN , and NH_3 interpolated from a pre-computed grid parametrized with temperature, pressure, C/O ratio, and [M/H]. We use a wide uniform prior in both C/O ratio ($0.1\text{--}1.5$) and [M/H] ($-2\text{--}3$). In this parametrization, the C/H ratio is fixed by the [M/H] value (using solar values from Asplund et al. 2009), while the O/H ratio is computed by the ratio of the C/H to the C/O.

We obtain consistent results across both reductions and resolutions, inferring a sub-Solar metallicity and a sub-Solar C/O ratio, with values of $[\text{M/H}] = -0.42^{+0.48}_{-0.38}$ and $\text{C/O} = 0.28^{+0.17}_{-0.12}$ from the Eureka! $R = 400$ reduction, depicted in Fig. 5. We also infer cool limb temperatures of $1010^{+110}_{-70}\text{ K}$, as is commonly observed in transmission spectroscopy retrievals (MacDonald et al. 2020; Welbanks & Madhusudhan 2022), and poor constraints on the cloud-top pressure (with a peak in the posterior at 10 mbar - see Fig. A1). We see evidence for H_2O and CO_2 at 3.3 and 2.1σ significance respectively.

The Eureka! reduction is consistent with no detector offset, while the Tiberius reduction has a median detector offset of $-56\pm 35\text{ ppm}$. Considering the metallicity posterior in Fig. A1 highlights a degeneracy present in the Tiberius reduction, with a lower evidence secondary mode with high metallicity ($\sim 60\times$ solar) and a large $\sim 110\text{ ppm}$ detector offset. This degeneracy is far weaker in the Eureka! reduction, only representing a slight tail in the posterior metallicity distribution rather than a second peak.

Repeating the retrievals on the $R = 400$ reductions with no offset, we confirm that no offset is necessary for the Eureka! reduction, slightly increasing the Bayesian evidence with a Bayes factor of 4.5, and removing the high metallicity tail, resulting in a somewhat tighter

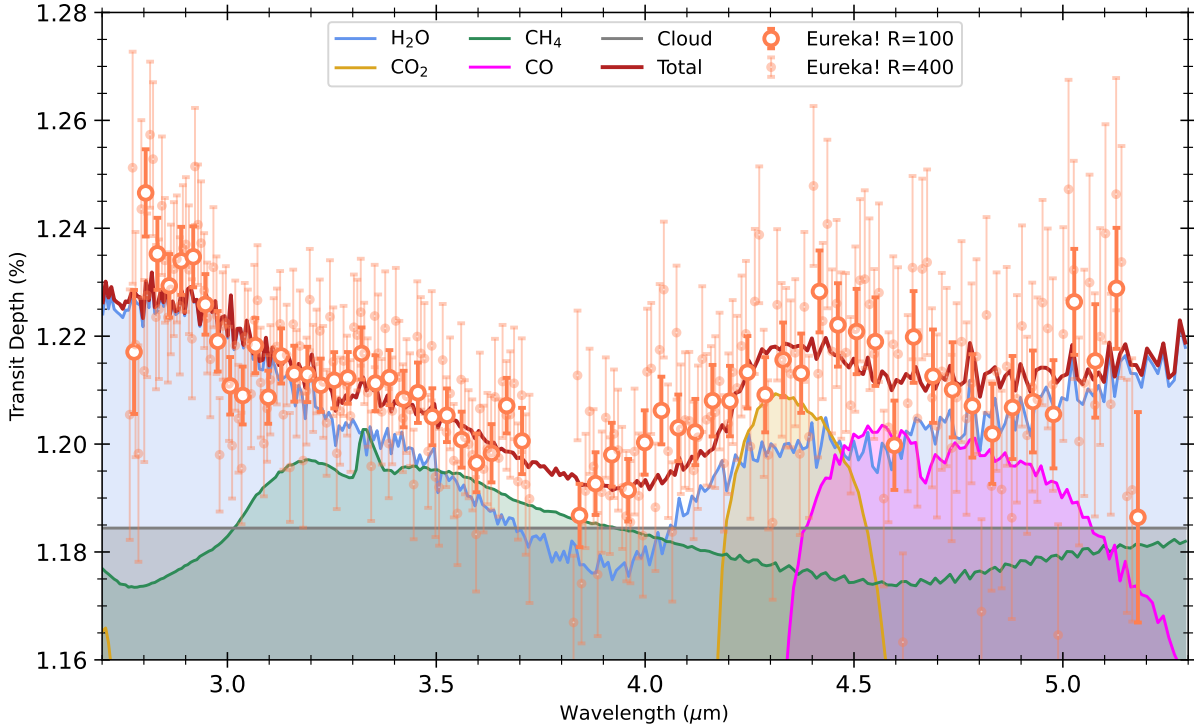


Figure 6. Median retrieved transmission spectrum of the Eureka! $R = 400$ data from the `petitRADTRANS` equilibrium chemistry retrieval convolved to a spectral resolution of $R = 400$, with the spectral contributions from H_2O , CO_2 , CH_4 , CO , and a grey cloud deck, and the combined absorption of all opacities (red).

posterior on the metallicity of $-0.39^{+0.30}_{-0.27}$. Not including an offset for the Tiberius reduction, on the other hand, is greatly disfavoured with a Bayes factor ($\frac{Z_1}{Z_2}$) of 1339, and gives discrepant results, with a lower C/O ratio, metallicity, and deeper clouds. We present this spectrum in Fig. 5, and the opacity contributions to this model in Fig. 6.

4.2.2 Free chemistry

For our free chemistry retrievals, the abundances of CH_4 , CO_2 , CO , H_2O , H_2S , SO_2 , and SO are free parameters, with a wide log-uniform prior in mass fraction from 10^{-12} to $10^{-0.5}$. We also tested retrievals including opacity from other species including NH_3 , HCN , OCS , CS_2 , and N_2O , but chose not to include them from our primary retrievals when the posteriors provided minimal constraints on their abundances. We obtain consistent results across all reductions and resolutions, retrieving a $\log(X_{\text{H}_2\text{O}})$ abundance of -3.3 ± 0.8 , and a $\log(X_{\text{CO}_2})$ abundance of $-8.1^{+0.9}_{-1.8}$ from the Eureka! $R = 400$ reduction. We also retrieve a very cold limb temperature of 650^{+120}_{-80} K, far cooler than the planet's equilibrium temperature of 1630 K. We place 2σ upper limits on the $\log(X_{\text{CH}_4})$ abundance of -6.1 , $\log(X_{\text{CO}})$ abundance of -3.6 , and $\log(X_{\text{SO}_2})$ abundance of -5.3 , respectively (see the posterior corner plot in Fig A3). There is also a strong peak in the posterior of the SO abundance at ~ 10 ppm, with a feature at $4.5 \mu\text{m}$, although repeating the retrievals without SO find its inclusion is slightly disfavoured by the Bayesian evidence, and it does not affect the other posteriors. The free retrieval abundance posteriors are consistent with the chemistry implied by the equilibrium retrievals above 100 mbar, as demonstrated in Fig. 7.

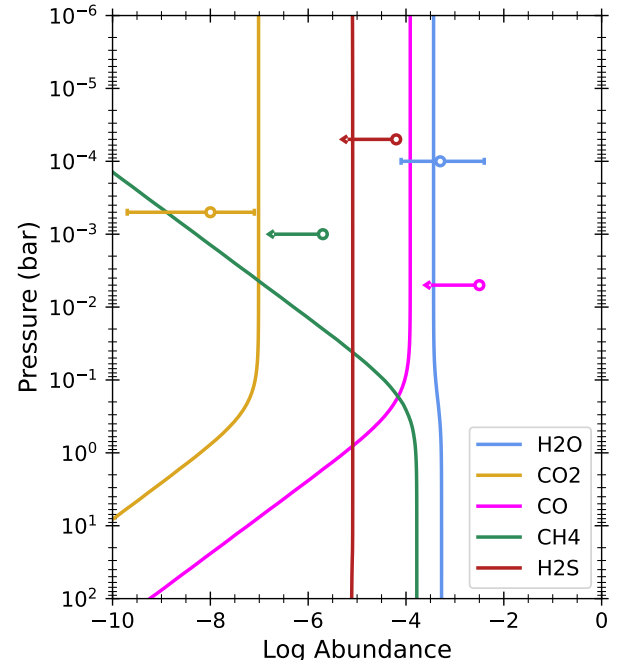


Figure 7. Vertical mixing ratios of H_2O , CO_2 , CH_4 , CO , and H_2S from the Eureka! $R = 400$ `petitRADTRANS` equilibrium chemistry retrieval (lines), plotted with the median retrieved abundances with 1σ error bars for the detected species (H_2O and CO_2), and upper limits from the other species (CH_4 , CO , and H_2S) from the free chemistry retrieval (data points).

4.2.3 Hybrid chemistry

In our hybrid chemistry retrievals, we combine the equilibrium chemistry approach to set the abundances of the carbon- and nitrogen-bearing species CH_4 , CO_2 , CO , H_2O , HCN , and NH_3 , parameterized with C/O ratio and [M/H], and the free chemistry approach to set the abundances of sulfur species H_2S , SO_2 , and SO to be free parameters. This allows us to model an atmosphere broadly in chemical equilibrium, but with the abundance of sulfur species modified by photochemistry or a variable S/O ratio.

Our hybrid chemistry results are broadly consistent with our equilibrium chemistry results, however, we do see stronger evidence for a high metallicity, high detector offset mode in both *Eureka!* and *Tiberius* reductions now, becoming the higher evidence mode in *Tiberius* $R = 400$. This appears to be caused by SO_2 , which has a notable peak in the posterior at ~ 1 ppm abundance. The abundances of H_2S and SO are unconstrained in the hybrid retrievals. All the hybrid retrievals have poorer evidence than their equilibrium chemistry counterparts. Each sulfur species added further decreases the evidence (disfavoured with a Bayes factor of 3 with all three species for the *Eureka!* reductions), except in the *Tiberius* $R = 400$ reduction, where the inclusion of SO_2 minimally improves the Bayesian evidence (Bayes factor of 1.3).

4.3 BeAR retrievals

We also perform retrievals using the open-source GPU-accelerated Bern Atmospheric Retrieval code (BeAR³) (Kitzmann et al. 2020). BeAR uses the MultiNest library (Feroz & Hobson 2008) to perform the retrieval using Bayesian nested-sampling (Skilling 2004), and using line-by-line opacity sampling. For our BeAR retrievals, we use a similar setup as in Kirk et al. (2025). We sample the opacities at a resolution of 0.1 cm^{-1} in wavenumber (equivalent to $R \sim 20,000$ – $30,000$), and include the following molecules and their associated ExoMol and HITRAN line-lists: H_2O (Polyansky et al. 2018), CH_4 (Yurchenko & Tennyson 2014), CO (Li et al. 2015), CO_2 (Yurchenko et al. 2020), H_2S (Azzam et al. 2016), SO_2 (Underwood et al. 2016), NH_3 (Coles et al. 2019), and HCN (Barber et al. 2014). All these opacities are computed using Helios-k (Grimm & Heng 2015) and are taken from the DACE database (Grimm et al. 2021). We also include opacity due to H_2 Rayleigh scattering (Cox 2000), and collision-induced absorption from H_2 – H_2 (Abel et al. 2011) and H_2 – He (Abel et al. 2012). The atmosphere is divided into 200 levels, equal in log-pressure space, ranging from 10 bar to 10^{-8} bar.

For the retrievals, the stellar radius is again fixed to $1.215 R_\odot$ (Bonomo et al. 2017). The planet's gravity and radius at the 10 bar pressure level are free parameters in the retrieval. The gravity has a gaussian prior on $\log g$ with a mean of 2.96 and a standard deviation of 0.03 in cgs units, and the radius has a uniform prior of 1.25 – $1.65 R_\text{J}$. The atmosphere is assumed to be isothermal, with a uniform prior on the temperature of 500–2500 K. A grey cloud deck is included, and the cloud-top pressure is a free parameter in the retrieval, with a log-uniform prior of 10^{-7} –1.0 bar. We also include an offset between the NRS1 and NRS2 detectors, with a uniform prior from -100 to +100 ppm.

We run two types of chemistry for our BeAR retrievals. Firstly, we assume free chemistry. In this retrieval, each molecule's volume mixing ratio is a free parameter, with a log-uniform prior from 10^{-12}

to 0.3. The mixing ratios are constant with altitude. The rest of the atmosphere is then filled with H_2 and He , in a solar ratio of 0.17 (Asplund et al. 2009). Secondly, we assume equilibrium chemistry. For this, the free parameters are the [M/H], which has a log-uniform prior of 0.1– $1000 \times$ solar, and the C/O ratio, which has a uniform prior of 0.1–2.0. [M/H] and C/O are related to the carbon and oxygen abundance in the same manner as in the *petitRADTRANS* models. The chemistry is calculated using *FastChem* (Stock et al. 2018, 2022), which is already integrated into BeAR. We apply both types of retrievals to the *Eureka!* and *Tiberius* spectra, and $R = 100$ and $R = 400$. The results of our chemical equilibrium and free chemistry retrievals with BeAR at $R = 400$ are shown in Figures A2 and A4, respectively.

In the equilibrium chemistry case, we see a good agreement across the two data reductions. The only difference occurs in the detector offset, for which the retrieval on the *Eureka!* reduction favours no offset, while the *Tiberius* reduction retrieval finds an offset of -60^{+23}_{-21} ppm. For the *Eureka* $R = 400$ retrieval, the retrieved [M/H] is $-0.52^{+0.31}_{-0.25}$, and the C/O ratio is $0.26^{+0.17}_{-0.11}$. The results are consistent with the *Tiberius* and $R = 100$ retrievals (see full results in Table A1).

In the free chemistry case, we again see a good agreement between *Eureka!* and *Tiberius* reductions, with the exception of a bimodality in the *Eureka!* $R = 100$ case. The alternative solution in the *Eureka!* case corresponds to an exceptionally high CO_2 abundance, which is compensated by a higher temperature, larger planet radius, lower water abundance, and a substantial negative offset of NRS2. However, at $R = 400$, the second solution in the *Eureka!* case is not present, and the retrievals agree with both the $R = 100$ and $R = 400$ *Tiberius* solution.

Finally, we also tested the effects of adding stellar contamination to our free chemistry retrievals. For this, we use the PHOENIX grid of stellar models (Husser et al. 2013), and set the stellar values to those in Table 1. We retrieve the stellar effective temperature, using a Gaussian prior with a mean of 6304 K and a standard deviation of 88 K (Johnson et al. 2011). We then include the effects of hot and cold spots on the star, and retrieve their temperatures and covering fractions. For the hot spots, the temperature is retrieved as a positive ΔT with respect to the stellar effective temperature, using a uniform prior of 0–1000 K. For the cold spots, the temperature is retrieved as a negative ΔT with respect to the stellar effective temperature, using a uniform prior of 0–1500 K. For both, the covering fractions use uniform priors of 0–0.5. For both reductions and resolutions, we find that adding stellar contamination to the retrievals has little effect on the results, and a Bayesian evidence comparison favours the retrieval without contamination in all cases except using the *Eureka!* reduction at $R = 100$. In the latter case, however, the Bayes factor is negligible at only 1.65. Overall we conclude that this constitutes no evidence for stellar contamination in the spectrum of HAT-P-30 b.

4.4 Overview of retrieval results

Using two independent retrieval analyses with *petitRADTRANS* and BeAR on two independent data reductions at two spectral resolutions, with a variety of retrieval setups, we are able to put together a consistent picture for the atmosphere of HAT-P-30 b. The complete set of results are presented in Table A1, with the posterior corner plots for the $R = 400$ retrievals displayed in Appendix A. We find that retrievals on the *Tiberius* reductions require an offset between the detectors, while the *Eureka!* reduction retrievals do not. We also generally find we get slightly tighter constraints using the

³ Formerly known at Helios-r2. BeAR can be found at <https://github.com/newstrangeworlds/bear>

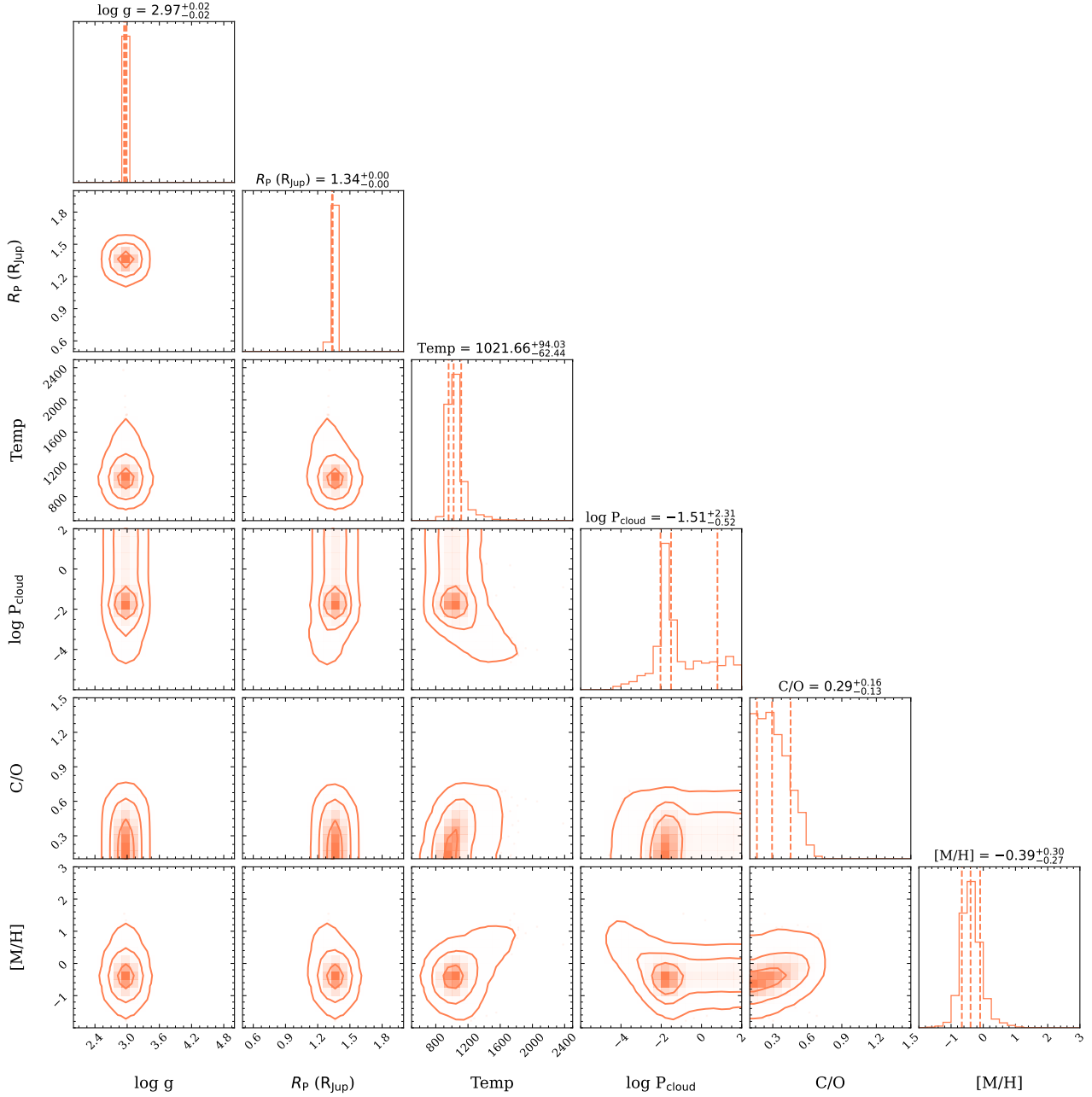


Figure 8. Corner plot showing the posterior probability distributions from the favoured retrieval setup: the `petitRADTRANS` equilibrium chemistry retrieval on the $R = 400$ Eureka! transmission spectrum with no detector offset.

$R = 400$ retrievals, given the better ability to sample narrow spectral features. Therefore we favour the interpretations from the Eureka! $R = 400$ retrieval with no offset. We present the median retrieved `petitRADTRANS` transmission spectrum to the Eureka! $R = 400$ spectrum in Fig. 5 with equilibrium chemistry and the posteriors for metallicity and C/O ratio, as well as the spectral contributions of each opacity source in Fig. 6, and the posterior corner plot in Fig. 8.

All the equilibrium retrievals have a consistent main result: sub-solar C/O ratio ($0.29^{+0.16}_{-0.13}$) and metallicity ($-0.39^{+0.30}_{-0.27} \times$ solar), with exact numbers taken from the `petitRADTRANS` Eureka! $R = 400$ equilibrium retrieval with no offset. The free chemistry retrievals are similarly concordant, and yield consistent abundances with those

implied by the equilibrium chemistry, with the vertical abundance profiles depicted in Fig. 7.

In a sub-sample of the retrievals, we do see a degree of bimodality, with an alternative explanation of a high-metallicity, CO₂-dominated spectrum. This secondary mode appears in the BeAR free retrieval of the Eureka! $R = 100$ spectrum, the `petitRADTRANS` equilibrium retrievals of both Tiberius spectra, and all the `petitRADTRANS` hybrid retrievals. The mode is highly degenerate with detector offset, requiring an offset of ~ 60 ppm in the Eureka! data and ~ 110 ppm in the Tiberius data. This mode represents a $50-100 \times$ solar metallicity, the lower end of which does fit within the constraints of a fully-mixed atmosphere from the interior structure modelling (see ahead to Section 5). This mode is only favoured over the low-metallicity

mode in a single retrieval, the *Tiberius* $R = 400$ *petitRADTRANS* hybrid retrieval. However, the evidence generally does not support the extra free parameters necessary for utilising a hybrid retrieval over equilibrium chemistry, and the ~ 110 ppm offset required is much larger than the typical offset observed in other data sets (e.g., Alderson et al. 2023; Moran et al. 2023). We therefore highly emphasize the lower metallicity mode as our favoured interpretation.

We also note that all of our free chemistry retrievals have very cold limb temperatures of ~ 650 K. Cool limb temperatures are commonly observed in transmission spectroscopy of hot Jupiters, and can be attributed to the 1D modelling of the atmosphere (MacDonald et al. 2020) (i.e. limb asymmetries) or the isothermal parametrization used (Welbanks & Madhusudhan 2022). This case, however, seems particularly extreme, with a 1000 K discrepancy from equilibrium temperature to observed isothermal temperature. We can see by comparing to the equilibrium chemistry retrievals, which are effectively forced into a higher temperature by the absence of CH_4 in the spectrum (the dominant carbon-carrier at low temperatures), that we may in fact be probing the cloud-top pressure-scale height degeneracy. The particular noise profile of the observation may be affecting the feature width and pushing us towards a low temperature explanation for the muted scale height, while in reality this is more likely an impact of clouds. This is demonstrated when restricting the temperature prior to higher temperatures, as the cloud top pressure is pushed higher to compensate. This does not impact our interpretation of the chemistry, however, as the abundances are consistent with the higher temperature equilibrium chemistry retrieval counterparts. A limb asymmetry analysis of the complete sample of BOWIE-ALIGN planets, including HAT-P-30 b, will be presented in future work.

We do note that the contribution from CH_4 appears to be non-negligible (see Fig. 6), despite CH_4 not being expected at the high temperatures of HAT-P-30 b. If the retrieved low temperature of HAT-P-30 b is a result of the temperature profile parametrization or limb asymmetry, the retrieval may then be trying to minimise the contribution from CH_4 by suppressing the carbon content of the planet, reflected as a low C/O ratio and metallicity. To account for this, we run an equilibrium retrieval discarding CH_4 as an opacity source. This results in a temperature posterior of ~ 650 K, matching the free retrievals, as the absence of strong CH_4 features no longer sets a lower limit on the temperature. We account for this by repeating the retrieval without CH_4 with a temperature lower bound of 1000 K. This results in a completely consistent best-fit spectrum to the equilibrium retrieval including CH_4 , although the constraints on temperature, cloud-top pressure, and metallicity are all weaker. We therefore demonstrate that rather than the low temperature driving the inclusion of CH_4 in the spectrum, it is in fact the other way around, with the enhanced opacity at $\sim 3.3 - 3.5 \mu\text{m}$ driving the retrieval to a lower temperature. We therefore do not believe that the low observed temperatures are suppressing the C/O ratio, but that our low temperature conclusion may instead be the result of enhanced transit depths at $\sim 3.3 - 3.5 \mu\text{m}$ from the particular random noise draw of this observation, the presence of disequilibrium CH_4 or species with similar opacity, or a non-grey continuum opacity putting in a bluewards-increasing slope in that wavelength range. We conclude that the observed sub-solar C/O ratio is robust, while the metallicity, while consistent with sub-solar, may be less well constrained ($-0.38^{+0.83}_{-0.68}$) than our equilibrium models suggest, should the real temperature be higher and the opacity discovered to not be CH_4 . Fixing the temperature at the equilibrium temperature of 1630 K biases the metallicity posterior towards the higher end of that distribution ($0.43^{+0.22}_{-0.46}$) but is still consistent with the nominal sub-solar metallicities within 2σ , while ruling out metallicities greater

than 10xSolar. The C/O ratio is unchanged by the fixed temperature, while the need for clouds around 0.1-1 mbar to sufficiently mute the spectral features becomes evident. The Bayesian evidence does not support fixing the temperature (decrease in $\ln Z$ of 6.7), and we note true temperature profile could very well diverge from an isotherm fixed to the equilibrium temperature.

For the purpose of studying the implications of our retrieved parameters for planet formation and relation to other planets in the BOWIE-ALIGN sample, we recommend the use of the posteriors from the *Eureka!* $R = 400$ *petitRADTRANS* retrieval with no offset between the detectors (Fig 8), as it is unimpacted by the degeneracy with the higher-metallicity mode. We therefore proceed with a C/O ratio of $0.29^{+0.16}_{-0.13}$ and metallicity of $-0.39^{+0.30}_{-0.27}$.

5 INTERIOR STRUCTURE MODELS

Using the Bayesian framework of Thorngren & Fortney (2019), we estimate the bulk composition of HAT-P-30 b, accounting for uncertainties in the mass, radius, and age of the planet. The evolution models underlying the statistical model are again from Thorngren & Fortney (2018), and solve the equations of hydrostatic equilibrium, conservation of mass, and the equation of state in one dimension. The planet's thermal state is evolved forward from a hot initial state using the atmosphere models of Fortney et al. (2007) to regulate heat flow out of the planet's interior. The equilibrium temperature is well into the hot Jupiter range, so we account for the anomalous heating using the flux-heating relation of Thorngren & Fortney (2018). This implies a quite high intrinsic temperature of 653 ± 45 .

The retrieval finds a bulk metallicity of $Z = 0.28 \pm 0.03$ (this is the statistical error from parameter uncertainties, not modeling uncertainty). This is within the expected range for a planet of this mass (Thorngren et al. 2016), being only moderately above average. If the planet were fully mixed, it would imply an atmospheric metallicity 2-sigma upper limit of $71.1 \times \text{Solar}$. The observed atmospheric metallicity could be less than this if the bulk metal is contained within a core or beneath a compositional gradient. It could not be greater, however, as this would be unstable to convection.

The substantial enhancement of the bulk metallicity relative to that observed in its atmosphere is not an inconsistency – it instead implies that the planet has a massive core. To match the radius and atmospheric metallicity, the core must be at least $50M_{\oplus}$. This could be either with a sharp core boundary or as a fuzzy core featuring an extensive compositional gradient (see e.g. Helled & Stevenson 2017) – structure models such as these don't distinguish between those cases (Bloot et al. 2023). A planet like this could have formed if most of the metal accretion occurred early on, with the final stages being the accretion of metal-poor gas. Alternatively, if the planet formed in the ice line, there might be a substantial quantity of rock and iron mixed into its interior that has either settled out or cannot be seen in the atmosphere due to condensation.

6 DISCUSSION

6.1 The atmosphere of HAT-P-30 b

Our transmission spectrum, obtained from two consistent independent reductions, describes the wavelength-dependent opacity in the atmosphere of HAT-P-30 b from $2.8 \mu\text{m}$ and $5.2 \mu\text{m}$ at a resolution of $R = 400$. We have used parametric radiative transfer models, implemented using atmospheric retrievals from the *petitRADTRANS* and BeAR retrieval packages, with a variety of retrieval setups including

equilibrium and free chemistry, to analyze this spectrum and make inferences about the atmospheric properties of HAT-P-30b. In 22 of the 23 retrievals performed, the favoured interpretation is one of a low-metallicity and C/O ratio atmosphere, representing sub-solar abundances of carbon and potentially also oxygen, derived from the equilibrium chemistry retrievals ($0.41^{+0.40}_{-0.19}$ and $0.77^{+0.84}_{-0.56} \times$ their solar abundances respectively, computed from the C/H, which is fixed by the metallicity, and the C/O ratio). In this interpretation, we require some muting of spectral features from cooler-than-expected temperatures (~ 1000 K in the equilibrium retrievals, ~ 650 K in the free retrievals due to the lack of chemical constraints) and clouds. No offset between detectors is favoured by the Bayesian evidence for the *Eureka!* spectra, while a ~ 55 ppm offset is required for the *Tiberius* spectra, matching the observed linear offset between the reductions. We see evidence for both H₂O and CO₂ at 3.3 and 2.1 σ respectively.

favoured in the *Tiberius* $R = 400$ *petitRADTRANS* hybrid chemistry retrieval, and present as a notable secondary mode in 4 other retrievals, is an alternative interpretation, with a highly super-solar metallicity of $\sim 60 \times$ solar. This is consistent with the upper limits of metallicity of a fully-mixed atmosphere suggested by our interior structure modelling. This mode requires freedom in both detector offset, needing a ~ 60 ppm offset in the *Eureka!* retrievals and ~ 110 ppm in the *Tiberius* retrievals, and SO₂ abundance, to appropriately fit the spectra with CO₂ features.

We favour the low metallicity interpretation for the atmosphere of HAT-P-30b for a number of reasons. Firstly, it is favoured in all of the standard equilibrium and free chemistry retrievals, and it is only not favoured with a single combination of reduction, resolution and retrieval pipeline, using the hybrid retrieval method - where the increase in complexity from the equilibrium method is not justified by the Bayesian evidence. Secondly, the large detector offset of 110 ppm that gives rise to the higher metallicity solution is greater than the offsets that have previously been present in NIRSpec/G395H observations of hot Jupiters (e.g., [Alderson et al. 2023](#)). Thirdly, the high metallicity modes only notably appears when the SO₂ abundance is a free parameter, to appropriately scale the transit depth at 4 μm . While SO₂ has been observed in exoplanet atmospheres (e.g., [Alderson et al. 2023](#)) and is predicted by photochemical models (e.g., [Tsai et al. 2023; Kirk et al. 2025](#)) in high metallicity hot Jupiters, including SO₂ does not improve the Bayesian evidence in all free retrievals, and 3 of 4 hybrid retrievals.

We therefore highly emphasize our low metallicity ($-0.39^{+0.30}_{-0.27}$) and C/O ratio ($0.29^{+0.16}_{-0.13}$) interpretation as that most favoured by our data and physical models. We do however note the existence of this physically-plausible alternative interpretation, with a high metallicity ($1.77^{+0.31}_{-0.07}$) and potential SO₂, representing a fully-mixed atmosphere, although we highlight it is by-in-large not favoured by our data. Further observations could definitively resolve between these scenarios, including NIRISS SOSS observations taken in March 2025 as part of JWST programme 5924 (PI: Sing). We also note that the apparent presence of CH₄ is somewhat impacting our interpretation of the chemistry and atmospheric temperature, and while this does not affect our inferred C/O ratio, disregarding CH₄ as a potential equilibrium opacity source does weaken the constraint on the metallicity to $-0.38^{+0.83}_{-0.68}$. We will investigate limb asymmetries of the BOWIE-ALIGN planets, a potential cause of the low observed temperature, in a future work, which could further refine our metallicity and temperature constraints.

6.2 Implications for formation

The preferred atmospheric retrieval solutions of HAT-P-30b show a sub-solar C/O ratio and sub-solar, sub-stellar metallicity with C/O = 0.18–0.38 and [M/H] = -0.83 to -0.05 , derived from *petitRADTRANS* equilibrium chemistry retrievals of the $R = 400$ *Eureka!* reduction. The C/O ratio deviates from the solar value at the $\sim 1.5 \sigma$ level. In formation models, supersolar metallicities and subsolar C/O are the expected outcome of high solid accretion of oxygen-rich dust and ice (e.g. [Madhusudhan et al. 2014](#)). However, we disfavour the high metallicity solutions with large detector offsets that appear in a subset of our retrievals (see Section 6.1).

Constraints from the C/O ratio and metallicity alone lead to large degeneracies in the possible formation history of the planet. However, a sub-solar C/O ratio and a sub-solar metallicity together are harder to reproduce because the gas in protoplanetary discs typically has sub-solar metallicity but super-solar C/O (see, e.g. [Bergin et al. 2024](#)). For this reason, the retrieved atmosphere is inconsistent with the fiducial models of [Penzlin et al. \(2024\)](#) by at least 1- σ . The closest match is for a planet that accreted most of its gas far from the star, where the gas is extremely metal-poor and all carbon and oxygen carriers are frozen out on the dust. Since the solid-phase abundance at this location has a solar C/O ratio, adding solids at this location produces an atmosphere with a solar C/O. If the planet accretes solids after migrating further in, this is no longer the case – the composition of solids can reach a sub-solar C/O ratio due to, e.g., the sublimation of CO and CH₄. Thus, by accreting gas far out but being enriched by a modest amount of solids as it migrates, a planet can reach sub-solar C/O ratios and metallicities in the outer disc in our models ([Penzlin et al. 2024](#)). Despite this, the fiducial simulations do not reach C/O ratios below 0.35 for sub-solar metallicity and, hence, exceed the best fit values of HAT-P-30b. This mismatch is, however, sensitive to the composition of the disc – the depletion of CO into CH₄ or C₂H₆ instead (e.g. [Bosman et al. 2019](#)) can lower the C/O ratio in the solids further and lead to a better agreement between models and observation.

As noted by [Meech et al. \(2025\)](#) when discussing TrES-4b (which has similar metallicity and C/O ratio to HAT-P-30b: $\log (Z/Z_{\odot}) = -0.41$ to -0.04 and C/O = 0.30–0.42), this is not the only possible channel of formation of sub-solar C/O and metallicities. Two further mechanisms allow a planet to reach sub-solar C/O and metallicity while migrating through the disc to a close-in orbit. In the first case, the abundances are dominated by the gas accreted. This requires the gas runaway phase of planet growth to happen just inside the water ice line (where the gas-phase C/O ratio can be sub-solar if the dust grains contain a significant amount of refractory carbon) and, therefore, accretes its bulk mass through water vapour-enriched gas and would predict that HAT-P-30b's metallicity is at most only slightly sub-stellar. The second case relies on accretion in an environment where the gas is depleted in metallicity by trapping volatile species in a dust trap further out in the disc.

TrES-4b differs from HAT-P-30b due to its orbital alignment: TrES-4b has an aligned orbit while HAT-P-30b is misaligned. If this difference in orbital alignment reflects an essential role of high-eccentricity migration in HAT-P-30b but not in TrES-4b, then TrES-4b will likely have migrated further through the disc to a close-in orbit and have probably accreted more gas and planetesimals in regions close to the star. This puts an additional caveat on the gas accretion-dominated scenario, in that the water snow line would have to be far enough out that HAT-P-30b formed inside the water snow line while remaining far enough out that high-eccentricity migration remains possible ($\gtrsim 0.6$ AU, [Muñoz et al. 2016](#)). As it stands, the

similarity in composition between TrES-4b and HAT-P-30 b may, or may not, point to similar formation histories despite their different migration history, making it difficult to draw strong conclusions by comparing them. However, with the full sample of eight planets in the BOWIE-ALIGN survey, we can make statistically more meaningful comparisons between the populations, hopefully gaining new insights into the formation of gas giants.

7 CONCLUSIONS

We present the JWST NIRSpec/G395H transmission of HAT-P-30 b, the fourth planet observed as part of the BOWIE-ALIGN programme, and one of four misaligned planets in the eight planet BOWIE-ALIGN sample. We use two independent data reductions and a host of atmospheric retrievals from two different pipelines to demonstrate a consistent interpretation for the planet's atmosphere. We find that HAT-P-30 b has a sub-solar metallicity of $0.41^{+0.40}_{-0.19} \times \text{solar}$ and a sub-solar C/O ratio of $0.29^{+0.16}_{-0.13}$. We detect H₂O (3.1 σ) and see evidence for CO₂ (2.1 σ), with consistent abundances between free and equilibrium chemistry retrievals, and evidence for muting of spectral features due to clouds and/or cool limb temperatures. We do not find evidence for stellar contamination or sulfur chemistry. We see no evidence for a detector offset in the *Eureka!* reduction, while we see a ~ 55 ppm detector offset between the detectors in the *Tiberius* reduction, becoming consistent with *Eureka!* with the free offset and therefore matching the observed linear offset between the reductions. We see evidence for a second possible atmospheric composition in a sub-set of the retrievals corresponding to a higher metallicity of $\sim 60 \times \text{solar}$, consistent with the upper limit of a fully-mixed atmosphere from our internal structure modelling. This alternative mode is favoured in only one of 23 performed retrievals, and is absent in most of the performed retrievals, requiring a larger offset (~ 110 ppm for *Tiberius*, ~ 65 ppm for *Eureka!*) and SO₂-abundance as a free parameter to adequately fit the observed transmission spectrum. We therefore strongly favour the low metallicity interpretation (discussed in more detail in Section 6.1), although we note that the metallicity constraints may be weaker depending on the cause of the low observed temperature.

The retrieved abundances suggest a composition similar to another BOWIE-ALIGN target, TrES-4 b (Meech et al. 2025), which has a metallicity of $0.58^{+0.59}_{-0.32} \times \text{solar}$ and a C/O of $0.32^{+0.11}_{-0.08}$, comparing *petitRADTRANS* equilibrium chemistry retrievals with identical setups. Obtaining a low metallicity and low C/O ratio deviates from the expected outcome of formation models, being inconsistent with Penzlin et al. (2024) by $> 1\sigma$. Several scenarios could explain this discrepancy, including accretion in the outer disc together with some CO depletion relative to the fiducial models, a composition dominated by gas accreted inside the water ice line, or accretion in a metallicity-depleted environment due to the trapping of volatile species further out in the disc. While HAT-P-30 b is misaligned in its orbit, TrES-4 b is aligned, suggesting that TrES-4 b may have migrated through disc migration rather than high-eccentricity migration. Given the constraints these migration mechanisms may place on the planet's evolution relative to the ice lines, we could very well be probing different explanations that give rise to similar atmospheric compositions. We therefore await the full BOWIE-ALIGN sample of eight planets to fully explore the formation of these two populations of hot Jupiters and draw statistically meaningful inferences. We do note that HAT-P-30 b has a significant difference in metallicity and C/O ratio compared to its fellow misaligned hot Jupiter WASP-15 b, demonstrating significant diversity can exist in planets with presumed similar formation histories.

ACKNOWLEDGEMENTS

This work is based on observations made with the NASA/ESA/CSA JWST. The data were obtained from the Mikulski Archive for Space Telescopes at the Space Telescope Science Institute, which is operated by the Association of Universities for Research in Astronomy, Inc., under NASA contract NAS 5-03127 for JWST. These observations are associated with program #3838. This work was inspired by collaboration through the UK-led BOWIE+ collaboration. Support for program JWST-GO-3838 was provided by NASA through a grant from the Space Telescope Science Institute, which is operated by the Association of Universities for Research in Astronomy, Inc., under NASA contract NAS 5-03127.

We thank the reviewer for improving the manuscript with their helpful comments. A.B.C acknowledges studentship support from the UK Science and Technology Facilities Council (STFC). C.E.F acknowledges financial support from the European Research Council (ERC) under the European Union's Horizon 2020 research and innovation program under grant agreement no. 805445. J.K acknowledges financial support from Imperial College London through an Imperial College Research Fellowship grant. A.P acknowledges funding from the European Union under the European Union's Horizon Europe Research and Innovation Programme 101124282 (EARLYBIRD). Views and opinions expressed are, however, those of the authors only and do not necessarily reflect those of the European Union or the European Research Council. Neither the European Union nor the granting authority can be held responsible for them. PJW acknowledges support from the UK Science and Technology Facilities Council (STFC) through consolidated grant ST/X001121/1. R.A.B thanks the Royal Society for their support through a University Research Fellowship. N.J.M., D.E.S. and M.Z. acknowledge support from a UKRI Future Leaders Fellowship [Grant MRT040866/1], a Science and Technology Facilities Funding Council Small Award [Grant ST/T000082/1], and the Leverhulme Trust through a research project grant [RPG-2020-82].

DATA AVAILABILITY

The raw data are available on the Mikulski Archive for Space Telescopes at the Space Telescope Science Institute, under program number #3838. The data products associated with this manuscript will also be made available on Zenodo.

REFERENCES

- Abel M., Frommhold L., Li X., Hunt K. L. C., 2011, *The Journal of Physical Chemistry A*, 115, 6805
- Abel M., Frommhold L., Li X., Hunt K. L. C., 2012, *J. Chem. Phys.*, 136, 044319
- Ahrer E.-M., et al., 2023, *Nature*, 614, 653
- Ahrer E.-M., et al., 2025, *Monthly Notices of the Royal Astronomical Society*, 543, 2442
- Albrecht S., et al., 2012, *The Astrophysical Journal*, 757, 18
- Alderson L., et al., 2023, *Nature*, 614, 664
- Alderson L., et al., 2024, *The Astronomical Journal*, 167, 216
- Asplund M., Grevesse N., Sauval A. J., Scott P., 2009, *Annual Review of Astronomy and Astrophysics*, 47, 481
- Azzam A. A., Tennyson J., Yurchenko S. N., Naumenko O. V., 2016, *Monthly Notices of the Royal Astronomical Society*, 460, 4063
- Barber R., Strange J., Hill C., Polyansky O., Mellau G. C., Yurchenko S., Tennyson J., 2014, *Monthly Notices of the Royal Astronomical Society*, 437, 1828

Bell T. J., et al., 2022, *JOSS*, 7, 4503

Bergin E. A., et al., 2024, *The Astrophysical Journal*, 965, 147

Beyer A., White R., 2024, *American Astronomical Society Meeting Abstracts*, 243, 205.08

Blažek M., et al., 2022, *MNRAS*, 513, 3444

Bloot S., Miguel Y., Bazot M., Howard S., 2023, *Monthly Notices of the Royal Astronomical Society*, 523, 6282

Bonomo A. S., et al., 2017, *A&A*, 602, A107

Booth R. A., Clarke C. J., Madhusudhan N., Ille J. D., 2017, *MNRAS*, 469, 3994

Borysow A., 2002, *Astronomy & Astrophysics*, 390, 779

Borysow J., Frommhold L., Birnbaum G., 1988, *Astrophysical Journal, Part 1 (ISSN 0004-637X)*, vol. 326, March 1, 1988, p. 509-515. NASA-supported research., 326, 509

Borysow A., Jørgensen U. G., Fu Y., 2001, *Journal of Quantitative Spectroscopy and Radiative Transfer*, 68, 235

Bosman A. D., Banzatti A., Bruderer S., Tielen A. G., Blake G. A., van Dishoeck E. F., 2019, *Astronomy & Astrophysics*, 631, A133

Brady R. P., Yurchenko S. N., Tennyson J., Kim G.-S., 2024, *Monthly Notices of the Royal Astronomical Society*, 527, 6675

Buchner J., et al., 2014, *Astronomy & Astrophysics*, 564, A125

Carter A., et al., 2024, *Nature Astronomy*, 8, 1008

Cegla H., et al., 2023, *Astronomy & Astrophysics*, 674, A174

Chan Y., Dalgarno A., 1965, *Proceedings of the Physical Society*, 85, 227

Coles P. A., Yurchenko S. N., Tennyson J., 2019, *Monthly Notices of the Royal Astronomical Society*, 490, 4638

Cox A. N., 2000, *Allen's astrophysical quantities*

Dalgarno A., Williams D., 1962, *Astrophysical Journal*, vol. 136, p. 690-692, 136, 690

Espinoza N., Fortney J. J., Miguel Y., Thorngren D., Murray-Clay R., 2017, *ApJ*, 838, L9

Feinstein A. D., et al., 2023, *Nature*, 614, 670

Feroz F., Hobson M. P., 2008, *MNRAS*, 384, 449

Foreman-Mackey D., Hogg D. W., Lang D., Goodman J., 2013, *Publications of the Astronomical Society of the Pacific*, 125, 306

Fortney J. J., Marley M. S., Barnes J. W., 2007, *The Astrophysical Journal*, 659, 1661

Grant D., Wakeford H. R., 2024, arXiv preprint arXiv:2408.10341

Grimm S. L., Heng K., 2015, *ApJ*, 808, 182

Grimm S. L., et al., 2021, *ApJS*, 253, 30

Helled R., Stevenson D., 2017, *The Astrophysical Journal Letters*, 840, L4

Helling C., et al., 2016, *MNRAS*, 460, 855

Horne K., 1986, *Publications of the Astronomical Society of the Pacific*, 98, 609

Husser T. O., Wende-von Berg S., Dreizler S., Homeier D., Reiners A., Barman T., Hauschildt P. H., 2013, *A&A*, 553, A6

Ivshina E. S., Winn J. N., 2022, *ApJS*, 259, 62

JWST Transiting Exoplanet Community Early Release Science Team et al., 2023, *Nature*, 614, 649

Jakobsen P., et al., 2022, *A&A*, 661, A80

Jeffreys H., 1939, *Theory of Probability*

Johnson J. A., et al., 2011, *ApJ*, 735, 24

Kirk J., Wheatley P. J., Louden T., Doyle A. P., Skillen I., McCormac J., Irwin P. G. J., Karjalainen R., 2017, *MNRAS*, 468, 3907

Kirk J., et al., 2021, *AJ*, 162, 34

Kirk J., et al., 2024a, *RAS Techniques and Instruments*, 3, 691

Kirk J., et al., 2024b, *AJ*, 167, 90

Kirk J., et al., 2025, *Monthly Notices of the Royal Astronomical Society*, p. staf208

Kitzmann D., Heng K., Oreshenko M., Grimm S. L., Apai D., Bowler B. P., Burgasser A. J., Marley M. S., 2020, *ApJ*, 890, 174

Kraft R. P., 1967, *ApJ*, 150, 551

Kreidberg L., 2015, *PASP*, 127, 1161

Law C. J., et al., 2021a, *The Astrophysical Journal Supplement Series*, 257, 3

Law C. J., et al., 2021b, *ApJS*, 257, 3

Li G., Gordon I. E., Rothman L. S., Tan Y., Hu S.-M., Kassi S., Campargue A., Medvedev E. S., 2015, *ApJS*, 216, 15

Ligterink N. F., Kipfer K., Gavino S., 2024, *Astronomy & Astrophysics*, 687, A224

MacDonald R. J., Goyal J. M., Lewis N. K., 2020, *ApJ*, 893, L43

Madhusudhan N., Amin M. A., Kennedy G. M., 2014, *ApJ*, 794, L12

Magic Z., Chiavassa A., Collet R., Asplund M., 2015, *A&A*, 573, A90

Meech A., et al., 2025, *Monthly Notices of the Royal Astronomical Society*, p. staf530

Mollière P., Wardenier J., Van Boekel R., Henning T., Molaverdikhani K., Snellen I., 2019, *Astronomy & Astrophysics*, 627, A67

Mollière P., et al., 2022, *The Astrophysical Journal*, 934, 74

Moran S. E., et al., 2023, *The Astrophysical Journal Letters*, 948, L11

Morbidelli A., et al., 2016, *Icarus*, 267, 368

Muñoz D. J., Lai D., Liu B., 2016, *MNRAS*, 460, 1086

Müller S., Helled R., 2024, *The Astrophysical Journal*, 967, 7

Nasedkin E., Mollière P., Blain D., 2024, *Journal of Open Source Software*, 9, 5875

Öberg K. I., Murray-Clay R., Bergin E. A., 2011, *ApJ*, 743, L16

Owen J. E., 2020, *MNRAS*, 495, 3160

Penzlin A. B. T., et al., 2024, *Monthly Notices of the Royal Astronomical Society*, 535, 171

Polyansky O. L., Kyuberis A. A., Zobov N. F., Tennyson J., Yurchenko S. N., Lodi L., 2018, *Monthly Notices of the Royal Astronomical Society*, 480, 2597

Rasio F. A., Ford E. B., 1996, *Science*, 274, 954

Rothman L. S., et al., 2010, *Journal of Quantitative Spectroscopy and Radiative Transfer*, 111, 2139

Rustamkulov Z., et al., 2023, *Nature*, 614, 659

Schneider A. D., Bitsch B., 2021, *A&A*, 654, A71

Skilling J., 2004, Bayesian inference and maximum entropy methods in science and engineering, 735, 395

Stock J. W., Kitzmann D., Patzer A. B. C., Sedlmayr E., 2018, *MNRAS*, 479, 865

Stock J. W., Kitzmann D., Patzer A. B. C., 2022, *MNRAS*, 517, 4070

Teske J., et al., 2025, *The Astronomical Journal*, 169, 249

Thorngren D. P., Fortney J. J., 2018, *AJ*, 155, 214

Thorngren D., Fortney J. J., 2019, *ApJ*, 874, L31

Thorngren D. P., Fortney J. J., Murray-Clay R. A., Lopez E. D., 2016, *ApJ*, 831, 64

Tsai S.-M., et al., 2023, *Nature*, 617, 483

Underwood D. S., Tennyson J., Yurchenko S. N., Huang X., Schwenke D. W., Lee T. J., Clausen S., Fateev A., 2016, *Monthly Notices of the Royal Astronomical Society*, 459, 3890

Wallack N. L., et al., 2024, *The Astronomical Journal*, 168, 77

Welbanks L., Madhusudhan N., 2022, *ApJ*, 933, 79

Winn J. N., Fabrycky D., Albrecht S., Johnson J. A., 2010, *The Astrophysical Journal*, 718, L145

Wu Y., Murray N., 2003, *ApJ*, 589, 605

Xue Q., Bean J. L., Zhang M., Welbanks L., Lunine J., August P., 2024, *The Astrophysical Journal Letters*, 963, L5

Yurchenko S. N., Tennyson J., 2014, *MNRAS*, 440, 1649

Yurchenko S. N., Amundsen D. S., Tennyson J., Waldmann I. P., 2017, *Astronomy & Astrophysics*, 605, A95

Yurchenko S., Mellor T. M., Freedman R. S., Tennyson J., 2020, *Monthly Notices of the Royal Astronomical Society*, 496, 5282

APPENDIX A: FULL ATMOSPHERIC RETRIEVAL RESULTS

We provide additional information from the atmospheric retrieval analysis described in Section 4. Table A1 summarizes the results from all 23 retrievals performed, while the corner plot of posterior probability distributions for the $R = 400$ equilibrium results from *petitRADTRANS* and *BeAR* are presented in Fig. A1 and Fig. A2 respectively, and the $R = 400$ free chemistry results are presented in Fig. A3 and Fig. A4.

Table A1. Retrieval results from `petitRADTRANS` and `BeAR`, as described in Section 4. For posteriors with reasonably well-formed peaks in their posteriors we provide the median and 1σ confidence intervals, for unconstrained parameters, we provide the 2σ upper limits. Parameters which weren't fitted in the retrieval model are marked with ‘-’.

Input spectrum	$\ln Z$	R_P (R _J)	$\log g$ (cgs)	T_{iso} (K)	$\log P_{\text{cloud}}$ (bar)	C/O	[M/H]	H ₂ O	CO ₂	CO	CH ₄	SO ₂	SO	Offset (ppm)
petitRADTRANS														
<i>Equilibrium Chemistry:</i>														
Eureka! $R = 100$	476.5 ± 0.3	1.337 ± 0.003	2.96 ± 0.02	1025^{+80}_{-59}	$-1.20^{+2.17}_{-0.83}$	$0.29^{+0.18}_{-0.13}$	$-0.47^{+0.42}_{-0.38}$	-	-	-	-	-	-	8 ± 31
Eureka! $R = 400$	1797.8 ± 0.1	1.336 ± 0.004	2.96 ± 0.02	1026^{+110}_{-68}	$-1.41^{+2.26}_{-0.97}$	$0.28^{+0.17}_{-0.12}$	$-0.42^{+0.48}_{-0.38}$	-	-	-	-	-	-	3 ± 30
Tiberius $R = 100$	474.5 ± 0.1	1.338 ± 0.005	2.96 ± 0.02	1014^{+106}_{-73}	$-1.63^{+2.31}_{-0.80}$	$0.30^{+0.19}_{-0.14}$	$-0.34^{+0.53}_{-0.44}$	-	-	-	-	-	-	-46 ± 36
Tiberius $R = 400$	1803.9 ± 0.1	1.337 ± 0.006	2.96 ± 0.02	1009^{+107}_{-69}	$-1.69^{+2.33}_{-0.66}$	$0.30^{+0.19}_{-0.13}$	$-0.29^{+0.63}_{-0.40}$	-	-	-	-	-	-	-56 ± 35
<i>Eq. Chemistry, no offset:</i>														
Eureka! $R = 400^{\dagger}$	1799.3 ± 0.1	1.336 ± 0.003	2.97 ± 0.02	1021^{+94}_{-62}	$-1.51^{+2.31}_{-0.52}$	$0.29^{+0.16}_{-0.13}$	$-0.39^{+0.30}_{-0.27}$	-	-	-	-	-	-	-
Tiberius $R = 400$	1796.7 ± 0.1	1.340 ± 0.003	2.96 ± 0.02	992^{+59}_{-48}	$0.07^{+1.34}_{-1.25}$	$0.18^{+0.11}_{-0.06}$	$-0.83^{+0.26}_{-0.32}$	-	-	-	-	-	-	-
<i>Free Chemistry:</i>														
Eureka! $R = 100$	477.0 ± 0.4	1.341 ± 0.004	2.96 ± 0.02	668^{+110}_{-86}	$0.61^{+0.92}_{-0.99}$	-	-	-3.2 ± 0.9	$-8.9^{+1.3}_{-2.6}$	< -3.0	< -5.9	< -5.1	$-5.0^{+1.0}_{-2.9}$	-5 ± 24
Eureka! $R = 400$	1798.0 ± 0.1	1.342 ± 0.004	2.96 ± 0.02	666^{+115}_{-81}	$0.50^{+0.95}_{-0.96}$	-	-	-3.3 ± 0.8	$-8.1^{+0.9}_{-1.8}$	< -3.6	< -6.1	< -5.3	$-5.4^{+1.2}_{-2.5}$	-11 ± 24
Tiberius $R = 100$	474.6 ± 0.1	1.345 ± 0.005	2.96 ± 0.02	672^{+126}_{-90}	$0.43^{+0.97}_{-1.02}$	-	-	$-3.5^{+0.9}_{-0.8}$	$-8.7^{+1.2}_{-2.4}$	< -3.1	< -4.1	< -5.9	$-5.2^{+1.0}_{-2.9}$	-55 ± 23
Tiberius $R = 400$	1805.6 ± 0.1	1.344 ± 0.004	2.96 ± 0.02	650^{+117}_{-77}	$0.52^{+0.96}_{-1.03}$	-	-	-3.4 ± 0.8	$-7.9^{+0.9}_{-1.4}$	< -2.7	< -5.9	< -5.5	< -2.6	-66 ± 24
<i>Free Chemistry, no SO:</i>														
Eureka! $R = 400$	1797.6 ± 0.1	1.342 ± 0.005	2.96 ± 0.02	686^{+123}_{-86}	$0.56^{+0.89}_{-0.97}$	-	-	$-3.3^{+0.9}_{-0.8}$	$-8.0^{+0.9}_{-1.7}$	< -2.5	< -5.7	< -5.6	-	-3 ± 24
<i>Hybrid Chemistry:</i>														
Eureka! $R = 100$	475.4 ± 0.1	1.336 ± 0.006	2.96 ± 0.02	1008^{+74}_{-68}	$-0.25^{+1.49}_{-1.46}$	$0.29^{+0.16}_{-0.12}$	$-0.36^{+2.09}_{-0.41}$	-	-	-	-	$-6.4^{+0.6}_{-3.6}$	< -3.3	-10 ± 44
Eureka! $R = 400$	1796.9 ± 0.1	1.333 ± 0.007	2.96 ± 0.02	1019^{+124}_{-78}	$-1.70^{+1.78}_{-0.68}$	$0.31^{+0.18}_{-0.13}$	$-0.05^{+1.96}_{-0.52}$	-	-	-	-	< -3.3	< -2.9	-32 ± 40
Tiberius $R = 100$	474.1 ± 0.2	1.336 ± 0.006	2.96 ± 0.02	981^{+93}_{-76}	$-0.91^{+1.92}_{-1.43}$	$0.28^{+0.16}_{-0.13}$	$-0.16^{+2.07}_{-0.49}$	-	-	-	-	< -3.8	< -1.8	-70 ± 47
Tiberius $R = 400$	1803.5 ± 0.1	1.329 ± 0.006	2.96 ± 0.02	989^{+123}_{-95}	$-1.66^{+2.32}_{-0.71}$	$0.34^{+0.16}_{-0.14}$	$1.77^{+0.31}_{-2.07}$	-	-	-	-	< -3.8	< -1.6	-116 ± 39
BeAR														
<i>Equilibrium Chemistry:</i>														
Eureka! $R = 100$	-354.8 ± 0.1	1.256 ± 0.003	2.96 ± 0.02	998^{+58}_{-51}	$-1.75^{+0.41}_{-0.24}$	$0.3^{+0.19}_{-0.13}$	$-0.5^{+0.32}_{-0.26}$	-	-	-	-	-	-	-6 ± 26
Eureka! $R = 400$	-1522.3 ± 0.1	1.257 ± 0.003	2.96 ± 0.03	985^{+58}_{-46}	$-1.76^{+0.44}_{-0.26}$	$0.26^{+0.17}_{-0.11}$	$-0.52^{+0.31}_{-0.25}$	-	-	-	-	-	-	-4^{+23}_{-24}
Tiberius $R = 100$	-356.4 ± 0.1	$1.258^{+0.003}_{-0.004}$	$2.96^{+0.03}_{-0.02}$	974^{+62}_{-48}	$-1.84^{+0.36}_{-0.26}$	$0.26^{+0.19}_{-0.11}$	$-0.5^{+0.3}_{-0.27}$	-	-	-	-	-	-	-49^{+27}_{-23}
Tiberius $R = 400$	-1524.7 ± 0.1	1.259 ± 0.003	2.96 ± 0.02	969^{+56}_{-47}	$-1.9^{+0.27}_{-0.24}$	$0.25^{+0.18}_{-0.11}$	$-0.46^{+0.29}_{-0.27}$	-	-	-	-	-	-	-60^{+23}_{-21}
<i>Free Chemistry:</i>														
Eureka! $R = 100$	-354.8 ± 0.1	$1.278^{+0.013}_{-0.005}$	2.96 ± 0.03	688^{+245}_{-85}	$-0.63^{+0.4}_{-0.55}$	-	-	$-2.9^{+1.0}_{-1.7}$	$-7.6^{+6.9}_{-2.0}$	< -2.3	< -5.7	< -5.5	-	-3^{+25}_{-88}
Eureka! $R = 400$	-1521.2 ± 0.1	1.277 ± 0.004	2.96 ± 0.03	674^{+93}_{-76}	$-0.66^{+0.43}_{-0.57}$	-	-	-2.7 ± 1.0	$-7.5^{+1.2}_{-1.4}$	< -3.1	< -6.0	< -5.9	-	-1^{+23}_{-24}
Tiberius $R = 100$	-355.5 ± 0.1	$1.279^{+0.004}_{-0.005}$	2.96 ± 0.03	659^{+105}_{-77}	$-0.7^{+0.46}_{-0.56}$	-	-	$-2.9^{+0.9}_{-1.0}$	$-8.2^{+1.3}_{-1.9}$	< -3.8	< -6.1	< -6.1	-	-41^{+22}_{-24}
Tiberius $R = 400$	-1522.6 ± 0.1	$1.28^{+0.003}_{-0.004}$	2.96 ± 0.03	644^{+92}_{-70}	$-0.66^{+0.43}_{-0.57}$	-	-	-2.9 ± 1.0	$-7.4^{+1.0}_{-1.2}$	< -3.8	< -6.2	< -6.0	-	-58^{+22}_{-20}

[†] Favoured interpretation.

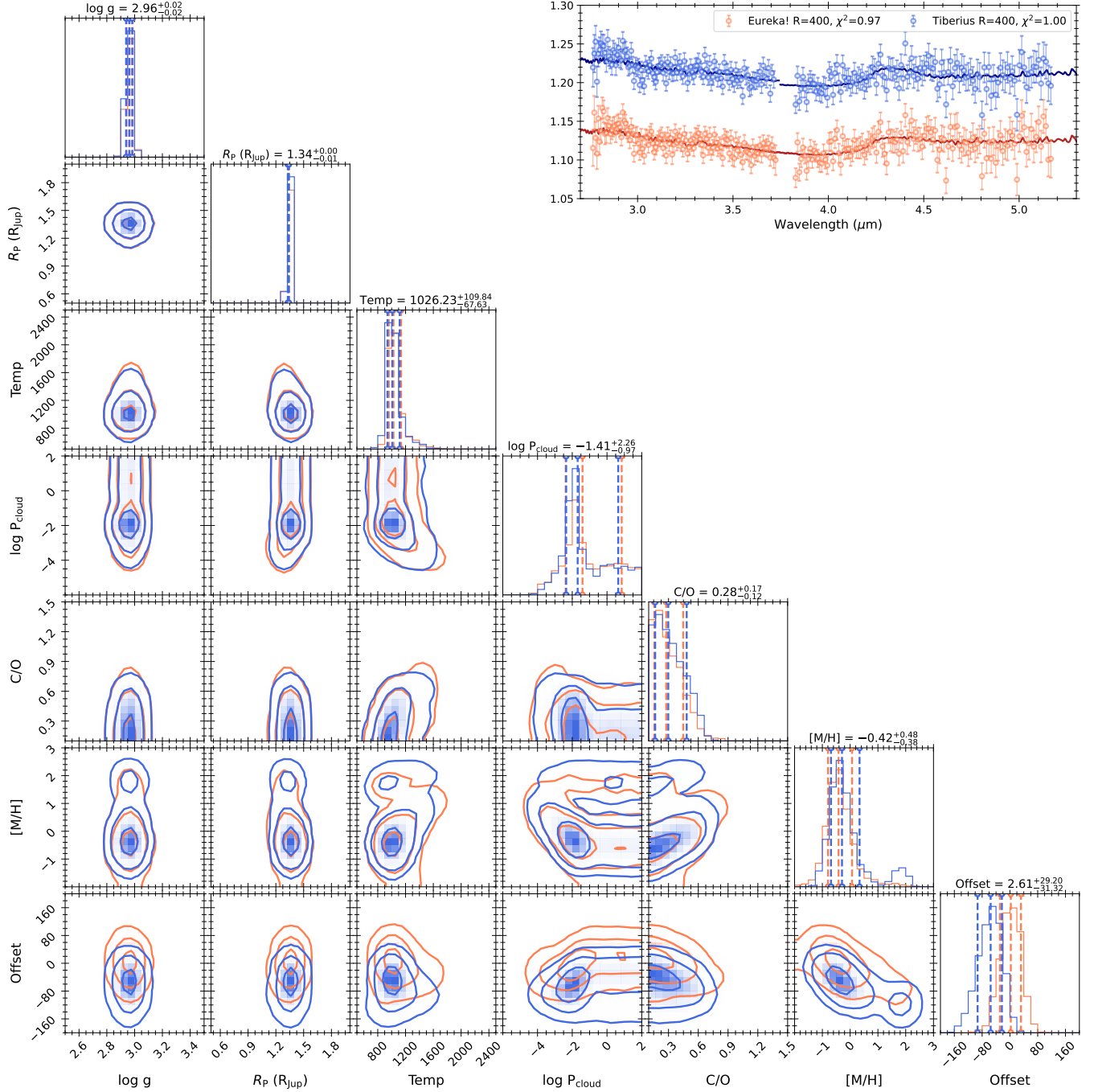


Figure A1. Corner plot showing the posterior probability distributions from the *petitRADTRANS* equilibrium chemistry retrievals on the $R = 400$ transmission spectra from Tiberius (blue) and Eureka! (orange, from which the numbers are derived). The top right panel displays the best-fit models from each retrieval, offset by 500 ppm, with the reduced χ^2 of the fit indicated in the legend.

This paper has been typeset from a $\text{\TeX}/\text{\LaTeX}$ file prepared by the author.

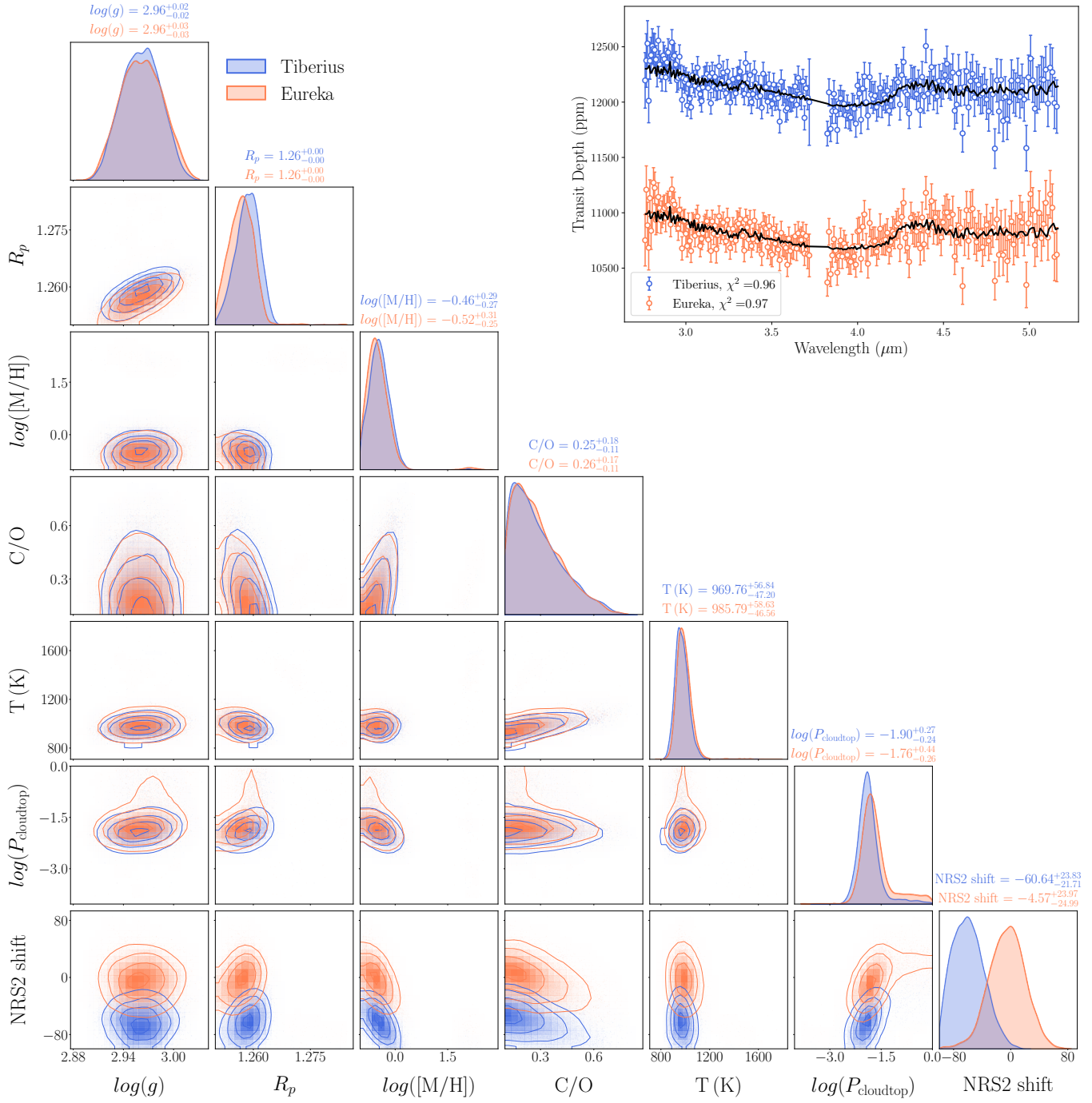


Figure A2. Cornerplot showing the posteriors from the BeAR chemical equilibrium retrievals on the Tiberius (blue) and Eureka! (orange) reductions of HAT-P-30 b at $R = 400$. The top right insert shows the best-fit models for the Tiberius (blue) and Eureka! (orange) reductions. The Eureka! spectrum is offset by 1300 ppm for visualisation purposes. The legend in the bottom left indicates the reduced χ^2 values for each of the fits.

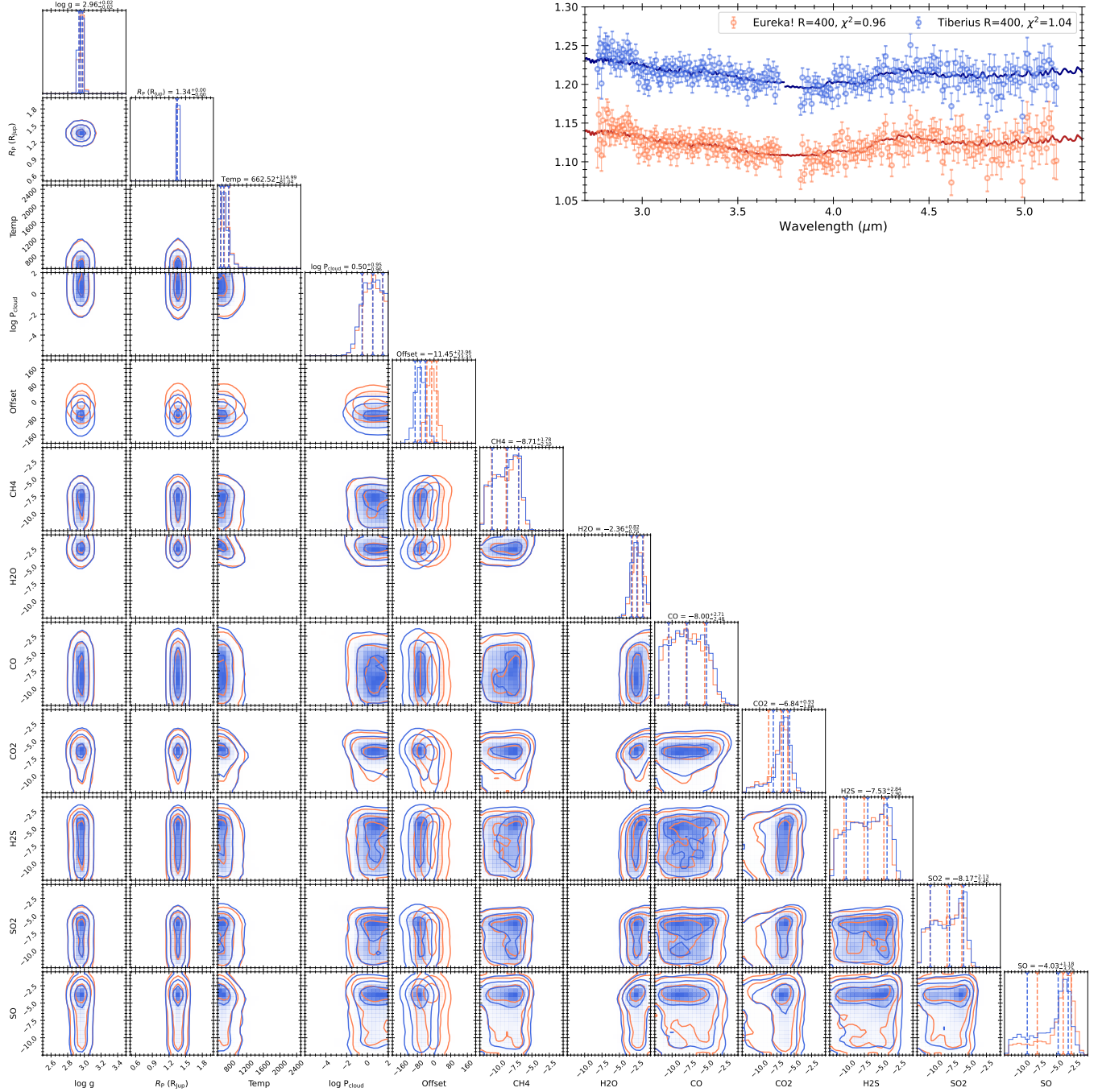


Figure A3. Corner plot showing the posterior probability distributions from the `petitRADTRANS` free chemistry retrievals on the $R = 400$ transmission spectra from Tiberius (blue) and Eureka! (orange, from which the numbers are derived). Abundances are given in units of logmass fractions. The top right panel displays the best-fit models from each retrieval, offset by 500 ppm, with the reduced χ^2 of the fit indicated in the legend.

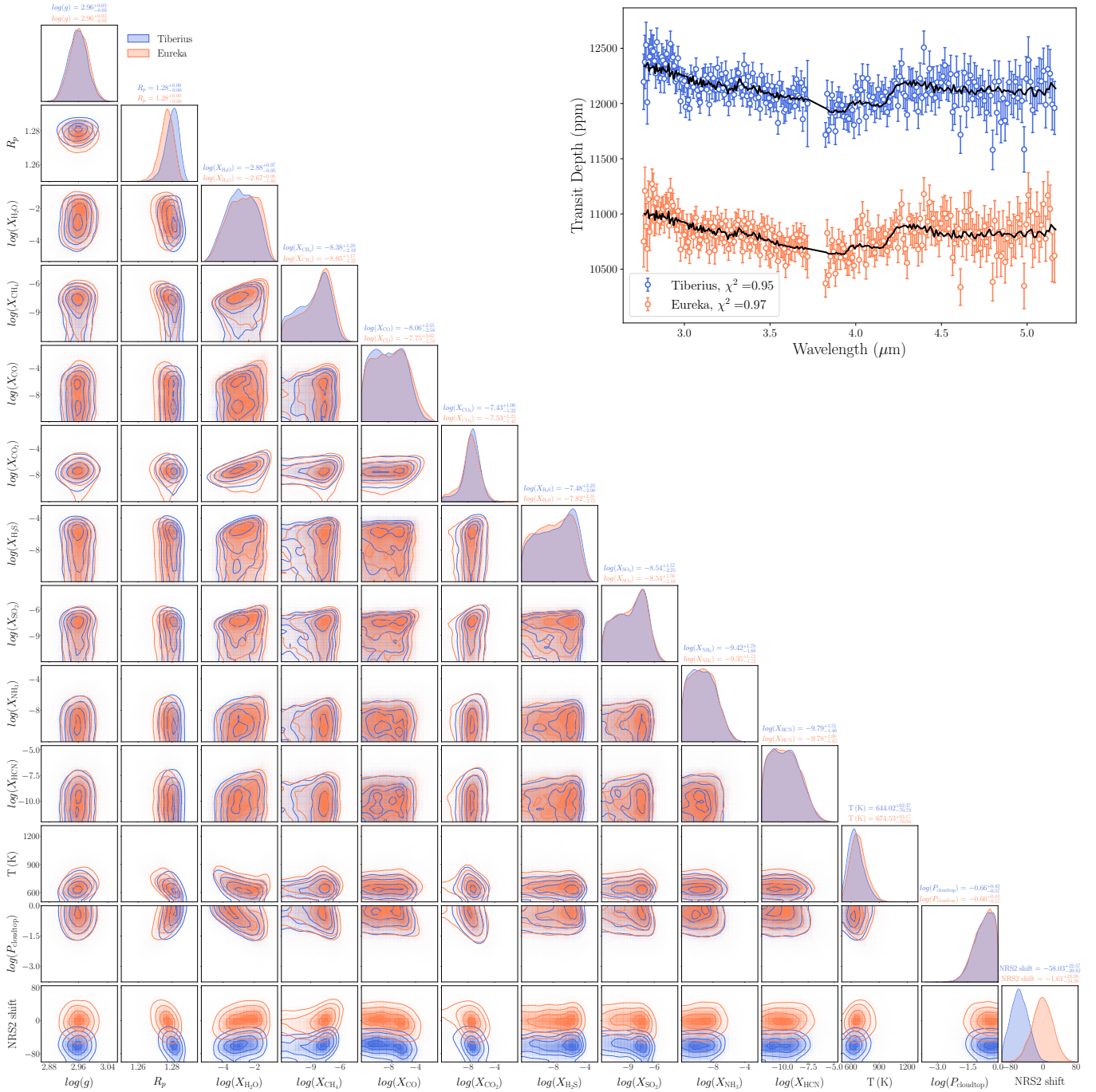


Figure A4. Cornerplot showing the posteriors from the BeAR free-chemistry retrievals on the Tiberius (blue) and Eureka! (orange) reductions of HAT-P-30 b at $R = 400$. Abundances are given in units of logvertical mixing ratios. The top right insert shows the best-fit models for the Tiberius (blue) and Eureka! (orange) reductions. The Eureka! spectrum is offset by 1300 ppm for visualisation purposes. The legend in the bottom left indicates the reduced χ^2 values for each of the fits.